processes

MDPI

Article

Rational Design of ZnGa-Sebacate/Graphene Nanoribbon Synergy for Effective Anticorrosive Polyurethane Coatings

Ujwal Mukkati Praveena, Michele Fedel and Stefano Rossi *

Department of Industrial Engineering, University of Trento, via Sommarive n. 9, 38123 Trento, Italy; u.mukkatipraveena@unitn.it (U.M.P.); michele.fedel@unitn.it (M.F.)
* Correspondence: stefano.rossi@unitn.it; Tel.: +39-0461-282403

Abstract

The development of hybrid organic coatings for corrosion protection remains a key research priority. This study focuses on synthesising Layered Double Hydroxide (ZnGa-LDHs) intercalated with environmentally friendly disodium sebacate (SB) corrosion inhibitor, forming ZnGa-SB. To overcome the challenge of limited dispersibility in organic coatings, ZnGa-SB was combined with Graphene Nanoribbons (GNR), produced through the oxidative unzipping of multi-walled carbon nanotubes (MWCNT). The resulting composite, ZnGa-SB/GNR, was synthesised using an in situ hydrothermal method and incorporated into polyurethane (PU) enamel. The synergy between high-barrier GNRs and active ZnGa-SB creates a "labyrinth effect" that effectively inhibits the diffusion of corrosive species. Microstructural analysis, including XRD, FT-IR, Raman, TGA, FE-SEM, and EDS, confirmed the nanofiller structure. The nanofillers were embedded into acrylic resin (AC) for short-term anticorrosive testing in a 0.1 M NaCl solution and then into PU for long-term evaluation in a 3.5 wt% NaCl solution, using electrochemical impedance spectroscopy (EIS). The PU/ZnGa-SB/GNR coating exhibited a high impedance modulus of 5.90×10^7 Ω cm^2 at $|Z|_{0.01}$ Hz, even after 2688 hours of immersion, indicating enhanced corrosion resistance. This coating demonstrated superior performance in cross-cut and pencil hardness tests and sustained less damage in salt spray analysis compared to other coatings. The synergistic effect offers a promising approach for developing next-generation hybrid anti-corrosive coatings.

Keywords: layered double hydroxide; graphene nanoribbon; sebacate; polyurethane coating; corrosion resistance

Academic Editors: Jesús Manuel Jáquez-Muñoz and Enrique Vera-López

Received: 19 December 2025
Revised: 19 January 2026
Accepted: 20 January 2026
Published: 23 January 2026

1. Introduction

Carbon steel is a crucial metal material widely used across various sectors of human activity and daily life [1,2]. However, environmental factors such as oxygen, water, and electrolytes can readily cause corrosion of carbon steel, leading to equipment degradation and reduced service life, posing significant safety risks [3]. Global estimates indicate that the annual cost of corrosion is approximately US $2.5 trillion, accounting for 3–6% of the world's gross domestic product (GDP) [4]. Considerable efforts have been made to prevent metal corrosion, including strategic material design [5], electrochemical protection [6], and the application of various corrosion inhibitors [7] and coatings [8]. Among these, inorganic, organic, and hybrid coatings are commonly used for corrosion protection due to their unique advantages, such as ease of preparation, high effectiveness, and durability [9]. In organic coatings, polyurethane (PU) coatings are recognised as one of the most effective

options for long-term protection of metal substrates in harsh environments, thanks to their excellent mechanical strength, chemical stability, and strong adhesion [10]. PU coatings form a protective barrier on metal surfaces, shielding them from corrosive agents like salts, moisture, and chemicals [11]. However, their protective efficacy can be compromised by mechanical damage, such as scratches or abrasions, which can expose the steel underneath to corrosive conditions [12]. This vulnerability has prompted substantial research to modify PU coatings to enhance their functionality and durability.

An innovative approach involves embedding nanoparticles or nanofillers within the polymeric matrix to improve its barrier and mechanical properties [13,14]. Typically, organic coatings are infused with specific types of nanofillers through two main methods: (i) directly adding active nanofillers into the coatings, such as phosphates [15], conducting polymers [16] and ferrite pigments [17]; and (ii) incorporating micro- or nano-containers containing inhibitors into the organic coatings, such as zirconia nanoparticles [18], halloysite nanotubes [19], layered double hydroxides (LDHs) [20], and silica nanocontainers [21], which are designed to release inhibitors in response to specific stimuli. Using nanocontainers loaded with inhibitors offers many advantages for organic coatings [22]. In contrast, directly embedding inhibitors into the coating may cause degradation due to negative interactions between the polymer matrix and active inhibitor species [23].

LDHs, a rapidly emerging category of two-dimensional materials, are attracting growing attention for use in protective coatings. This interest stems from their strong chemical stability, impressive barrier properties, and significant capacity for accommodating inhibitor species [24]. LDHs can efficiently release inhibitor ions from their interlayer spaces and capture chloride (Cl^-) ions from the corrosive electrolyte, thanks to their ion exchange capabilities [25,26]. Moreover, compared to other two-dimensional (2D) materials, LDHs provide greater design flexibility and are more cost-effective [27]. LDH has recently demonstrated novel applications in anti-friction [28], anti-wear [29], antibacterial [30] and corrosion resistance. R. Chen and coworkers [31] explored the use of NiGa LDH-based composite to investigate the photocathodic anticorrosion of 304 stainless steel. The presence of Ga^{3+} enhanced the composite's charge-separation efficiency, resulting in a more negative shift in the open-circuit potential of 304 stainless steel. Similarly, A. Akman and coworkers [32] investigated the effect of minor gallium addition on the corrosion behaviour of Ti-Nb alloys. The introduction of Ga^{3+} improved passive film resistance, likely due to the contribution of a Ga-based oxide to passive film growth. Additionally, Ga^{3+} is electrochemically inactive, thereby eliminating the risk of redox-induced coating degradation [33].

To enhance inhibitory properties, various organic and mineral inhibitors have been incorporated into LDH compositions [34]. Recent research has identified organic acid inhibitors as promising candidates among environmentally sustainable inhibitors, as they can intercalate into LDHs, indicating their potential as effective smart nanofillers [35]. G. Hefter and team investigated the straight-chain dicarboxylates for their anticorrosion properties against copper, aluminium, and mild steel under different conditions. The findings indicated that strain chain dicarboxylates could serve as excellent inhibitors for shielding the substrates. The degree of their effectiveness is determined by several factors, including chain length, number of carboxylate groups, pH and the nature of the electrolyte used [36,37]. Studies have explored the use of dicarboxylates with varying chain lengths, including adipate, Sebacate (SB), malonate and succinate, as potential corrosion inhibitors for steel in a neutral NaCl solution, both in the presence and absence of benzotriazole. SB, whether used alone or in conjunction with benzotriazole, demonstrated the highest level of inhibition efficiency [38], making it our interest for the study. SB are straight-chain aliphatic dicarboxylate molecules with a ten-carbon chain, known for forming complexes

with iron ions, which enables them to effectively compete with Cl^- ions and protect steel in near-neutral environments [39]. Despite several advantages of SB, its direct addition to the polymer matrix is discouraged due to potential reactions between the matrix and SB itself. To resolve this issue, the strategy involves using containers capable of storing the SB and releasing it when necessary, such as the LDH [40]. Although the LDH-inhibitor system offers many advantages, the high number of hydroxyl groups on the LDH surface leads to strong hydrogen bonding, resulting in poor dispersion of these nanocontainers within organic coatings. Researchers have extensively investigated methods to improve the dispersibility of such nanocontainers in organic coatings [41].

In this context, several strategies can be considered, such as integrating hybrid nanocarriers like LDH with other nanocarriers suitable for organic coatings, such as multi-walled carbon nanotubes (MWCNTs) and their derivatives. This approach not only effectively impedes corrosion but also improves the compatibility of LDH within organic coatings [42]. S. Rezaeifard and group [42] investigated the trisodium phosphate-loaded MgAl LDH/oxidised-MWCNT (T-MgAl/O-MWCNT) for smart epoxy anticorrosive applications. The composite reduced the corrosion current density of the steel due to the release of phosphate. Electrochemical Impedance Spectroscopy (EIS) analysis revealed a substantial increase in impedance at low-frequency values, indicating the enhanced barrier properties of the epoxy due to the good dispersion of T-MgAl/O-MWCNT. Similarly, another composite Mo-doped MgAl LDH/ functionalised MWCNT (SM-MgAl/FCN) was investigated by S. Rezaeifard and group [34]. The composite achieved a maximum corrosion prevention efficiency of approximately 90.88%, exhibited self-repairing behaviour, and demonstrated improved mechanical properties.

One notable derivative of MWCNT is the quasi-one-dimensional graphene-like material with a ribbon morphology, known as graphene nanoribbon (GNR). These nanofillers are characterised by their narrower width and high density of edge defect sites, which give them superior chemical reactivity. The large surface area of GNRs, along with the abundance of reactive edges and defects, makes them a promising candidate for nanofillers in anti-corrosive applications. However, unlike other carbonaceous materials, GNRs remain relatively underexplored as nanofillers in high-barrier coating applications [43].

To thoroughly understand the anticorrosive properties of various nanofillers, short-term assessments are necessary. These tests provide a foundation for future long-term studies. One effective method for such rapid evaluations involves incorporating nanofillers into a model organic coating. H.N. McMurray [44] and group evaluated the anticorrosive properties of different organic and inorganic inhibitors infused in LDHs by dispersing them in a model PVB coating. V33 Parquet Primer is an acrylic primer (AC) that serves as a suitable model organic coating for short-term testing of nanofillers' anticorrosive performance, thanks to its easy application, cost effectiveness and quick drying time.

Considering the factors discussed earlier, we developed a simple one-pot hydrothermal process to fabricate a sebacate-intercalated Zinc Gallium LDH/Graphene nanoribbon (ZnGa-SB/GNR) composite. For comparison, the individual nanofillers, such as ZnGa-SB, were synthesised via hydrothermal methods, while GNR was produced by oxidative unzipping of MWCNT. The morphology and chemical structures of these nanofillers were characterised using X-ray diffraction (XRD), Fourier transform infrared (FT-IR) spectroscopy, Raman spectroscopy, thermogravimetric analysis (TGA), field-emission scanning electron microscopy (FE-SEM), and energy-dispersive X-ray spectroscopy (EDS). These nanofillers were then incorporated into an AC model coating for short-term screening of their anticorrosive properties. The PU matrix, containing individual nanofillers and the composite, was tested to better understand the long-term inhibitory performance. The combination of GNR with ZnGa-SB nanoparticles aimed to enhance the compatibility of

the LDH layers within the PU matrix and facilitate the controlled release of the corrosion inhibitor. The barrier effectiveness of the nanofillers in the PU coating was assessed using electrochemical impedance spectroscopy (EIS), neutral salt spray analysis (NSSA), and adhesion tests. This approach presents a novel method for preparing nanofillers suitable for durable anticorrosive coatings, offering promising practical applications.

2. Experimental

2.1. Materials and Reagents

Zinc nitrate hexahydrate ($Zn(NO_3)_2 \cdot 6H_2O$, >98.0%), gallium nitrate hydrate ($Ga(NO_3)_3 \cdot xH_2O$, >98.0%), and multi-walled carbon nanotubes (MWCNTs, >98.0%) were all purchased from Sigma Aldrich, USA. Disodium sebacate ($C_{10}H_{18}O_4 \cdot 2Na$, >98.7%) was purchased from BLD-pharm (Germany). Sodium carbonate (Na_2CO_3, >99.0%) and sodium hydroxide (NaOH, >96.0%) were supplied by Carlo Ebra Reagents, Italy. Concentrated sulphuric acid (con. H_2SO_4, Panreac AppliChem, Spain), Potassium permanganate ($KMnO_4$, Fluka Chemie GmbH, Czech Republic), Hydrogen peroxide (H_2O_2, Sigma Aldrich, Germany), Concentrated hydrochloric acid (HCl, Panreac AppliChem, Germany). V33 057547 Colourless Parquet Sealer Primer (V33 Group, Italy), Emucril PU altas prestaciones (Pinturas Emucril, Spain), Catalizador Emucril PU altas prestaciones (component B, Pinturas Emucril, Spain), and Xylene (Merck eurolab, France) were also obtained.

2.2. Protocol for Fabricating the Nanofillers

2.2.1. Synthesis of ZnGa-CO_3^{2-} LDH

The synthesis of carbonate-intercalated zinc gallium-layered double hydroxide (ZnGa-CO_3^{2-}) was accomplished via a single-step hydrothermal process [45]. Initially, $Zn(NO_3)_2 \cdot 6H_2O$ (0.3 M) and $Ga(NO_3)_3 \cdot xH_2O$ (0.1 M) were dissolved in 50 mL of deionised water, followed by vigorous stirring to ensure the formation of a homogeneous solution, referred to as Solution A. In a separate beaker, NaOH (8 M) and Na_2CO_3 (4 M) were mixed with 100 mL of deionised water to form a uniform solution B. Subsequently, solution B was titrated against solution A at ambient temperature while maintaining continuous magnetic stirring of the mixture. During the titration, the pH of the resultant solution was maintained in the range of 9–10 using a 1 M NaOH solution. Following the completion of the titration, a dense white suspension was observed. This suspension was subjected to magnetic stirring for an additional 30 min before being transferred to a 200 mL Teflon-lined autoclave. The autoclave was then sealed and heated to 80 °C for 12 h. The resulting slurry was centrifuged at 5000 rpm, and the final solid content was washed with water and ethanol separately until a neutral pH was reached. Finally, the product was oven-dried at 60 °C for 12 h, and the obtained white powder was labelled ZnGa-CO_3^{2-} LDH.

2.2.2. Synthesis of ZnGa-SB LDH

The synthesis of sebacate-intercalated zinc gallium-layered double hydroxide (ZnGa-SB) is similar to that of ZnGa-CO_3^{2-} LDH. The Na_2CO_3 component in solution B was replaced with an equivalent amount of SB. Under the previously discussed hydrothermal conditions, solution B, which comprised SB anions, was titrated against solution A to facilitate the effective intercalation of SB into the interlayers of ZnGa-LDH. The final mixture was magnetically stirred for 24 h and then transferred to an autoclave for post-synthesis treatment. Throughout the titration reaction, nitrogen bubbling was performed to prevent any undesired intercalation of carbonate anions (derived from dissolved CO_2) into the interlayers of ZnGa-LDH.

2.2.3. Synthesis of GNR

Graphene nanoribbons (GNR) were synthesised through a two-step oxidative unzipping of multi-walled carbon nanotubes (MWCNTs) employing a modified version of the Hummers method [46]. In brief, 0.3 g of MWCNTs was combined with 150 mL of con. H_2SO_4, and the mixture was continuously stirred at ambient temperature for approximately 24 h, leading to the formation of a homogeneous slurry. Subsequently, 1.5 g of potassium permanganate ($KMnO_4$) was added gradually to the slurry over 30 min with continuous magnetic stirring. Following the addition of the oxidising agent, the mixture was heated to 85 °C and maintained at this temperature for 4 h. The hot slurry was diluted with 400 mL of deionised water and transferred to an ice bath for cooling. After 30 min, the slurry was removed from the ice bath, and 60 mL of 30% H_2O_2 solution was added. Subsequently, 200 mL of deionised water was added to the mixture to prevent the formation of insoluble manganese dioxide (MnO_2). The GNR mixture was cooled to room temperature, followed by sequential washing and centrifugation with 10% HCl until the pH approached the neutral range. Following repeated rinsing with deionised water and ethanol, the solid GNR residue was dried at 60 °C under vacuum to ensure the thorough removal of any remaining solvents. Upon completion of the vacuum drying process, the fine dark grey solid powder obtained was labelled as GNR.

2.2.4. Synthesis of ZnGa-SB/GNR

The GNR dispersion was prepared by incorporating GNR (1 mg/mL) into 100 mL of distilled water that had been saturated with nitrogen gas. Continuing to bubble nitrogen into the GNR mixture, an equivalent amount of SB was added. The pH of the mixture was raised to 9–10, using a 1 M NaOH solution and labelled solution B. After stirring for 30 min at ambient temperature, solution B was titrated against the previously prepared ZnGa solution (solution A). In parallel with the hydrothermal procedure and post-synthesis treatment outlined for the synthesis of ZnGa-SB LDH, the final precipitate was centrifuged, washed with water and ethanol several times, and oven-dried at 60 °C for 12 h (Figure 1). The final dark-grey powder obtained was labelled ZnGa-SB/GNR.

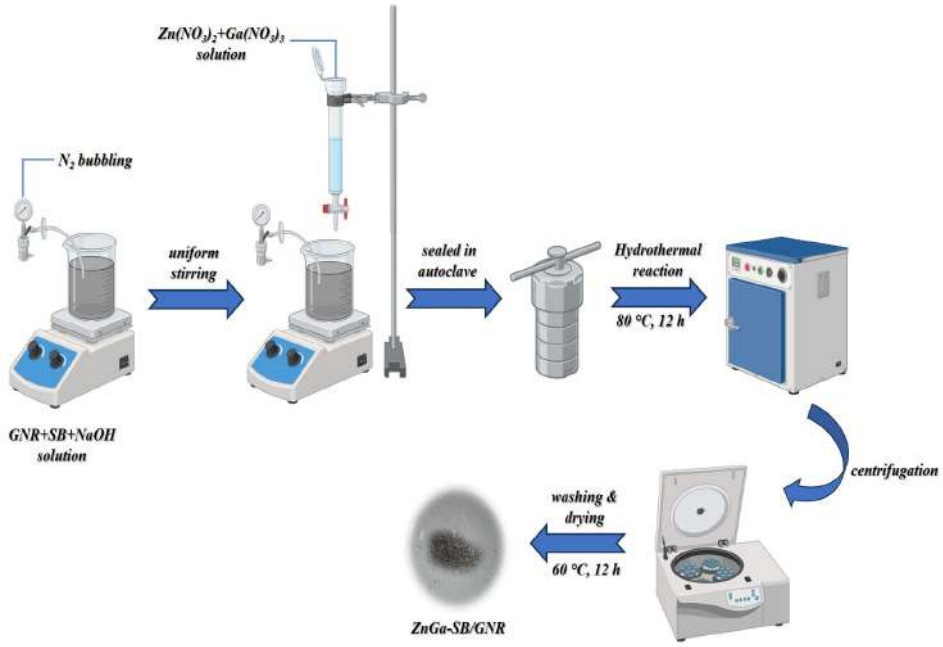

Figure 1. Schematic diagram for synthesising the designed ZnGa-SB/GNR nanofiller.

2.3. Protocol for Fabrication of Coatings

2.3.1. Preparation of Acrylic-Coated Steel Samples

The protective characteristics of different nanofillers, namely ZnGa-SB, GNR, and ZnGa-SB LDH/GNR, were investigated using a two-layer clearcoat (V33 057547 Colourless Parquet Sealer Primer, V33 Group, Italy) applied over steel samples. The two-layer coating strategy was designed to avert any potential leaching of particles towards the exterior of the coating. Initially, the R36 Q-Panel Steel A1008 surface was degreased in acetone, accompanied by ultrasonic agitation, for 5 minutes. Later, the steel surface was acid pickled using 2 M HCl for 15 min. The 1 wt% nanofillers, pre-sieved through a 60 μm mesh, were individually incorporated into the clear coat and subjected to ultrasonic agitation for 5 min to achieve uniform dispersion. These mixtures were then applied separately to the pre-treated steel surface via blade coating, utilising the automatic applier Elcometer 4340 (Elcometer Ltd., Manchester, UK), to achieve a 100 μm wet thickness primer layer. The coatings were cured at 60 °C for 24 h. Following this, a top coat was applied using only the clear coat, devoid of nanofillers, following the same procedure. The coated samples underwent an additional 24 h curing period at 60 °C, resulting in specimens designated as AC, AC/ZnGa-SB, AC/GNR, and AC/ZnGa-SB/GNR. The dry thickness of the cured coatings was determined to be 70 μm.

2.3.2. Preparation of Polyurethane-Coated Steel Samples

The surface of the R36 Q-Panel Steel A1008 was initially degreased in acetone using ultrasonic agitation for 5 min. Following this, the surface underwent acid pickling treatment with a 2 M HCl solution for 15 min. The different nano filler powders, i.e., ZnGa-SB, GNR and ZnGa-SB LDH/GNR, were sieved through a 60 μm mesh. The individual nano filler powders (1 wt%) were dispersed in 7 mL of component B and 3 mL of xylene, which served as a thinner. To these concoctions, 50 mL of Emucril PU-based acrylic resin (PU) was added separately and mixed thoroughly to prevent agglomeration and ensure uniform dispersion of pigments. Following the preparation, the mixtures were separately loaded into the spray gun and subsequently applied through spray painting onto the pretreated R36 Q-Panel Steel A1008 surface. Finally, the coated samples were cured at 30 °C for 24 h, and the resulting coated specimens were named PU, PU/ZnGa-SB, PU/GNR, and PU/ZnGa-SB/GNR. The dry thickness of the cured coatings was gauged as 60–75 μm.

2.4. Pigments Characterisation

The crystal structure of the nanofillers was analysed using powdered X-ray diffraction patterns, utilising an X'Pert High Score diffractometer manufactured by Rigaku, Japan. The instrument employed a Cu Kα emission source (λ = 1.5418 Å) configured with a monochromator set at 30 kV and 10 mA, covering a diffraction angle range of 2θ = 03°–80°. The chemical characterisation of the nanofillers was performed using Fourier transform infrared spectroscopy (FT-IR) in attenuated total reflectance mode, utilising a Perkin Elmer Spectrum One FTIR spectrometer (Perkin Elmer Inc., Shelton, CT, USA). The spectral range was from 4000 to 500 cm^{-1} with a resolution of 4 cm^{-1}. Raman spectroscopy was utilised in identifying the carbon structure using the LabRaman ARAMIS system from Horiba-Jobin-Yvon, operating at a wavelength of 633 nm. The thermal stability of the nanofillers was investigated using thermogravimetric analysis (TGA) with the NETZSCH STA 409 PC/PG instrument. The TGA instrument was operated in the temperature range of 20–900 °C under a nitrogen atmosphere, with a consistent heating rate of 10 °C min^{-1}. The surface morphology and elemental composition were examined using a Jeol JSM-IT300 (Japan) scanning electron microscope (SEM) equipped with an energy-dispersive X-ray spectroscopy (EDS) detector.

2.5. Anticorrosive Evaluations

2.5.1. Electrochemical Assessments

The inhibitory properties of different coatings containing nanofillers were evaluated using electrochemical impedance spectroscopy (EIS) with an Autolab 302 N potentiostat/galvanostat/FRA (Metrohm AG, Herisau, Switzerland). The EIS measurements were conducted in a three-electrode setup, where the coated steel panel acted as the working electrode, a platinum electrode served as the counter electrode, and an Ag/AgCl/3.5 mol/L KCl electrode was used as the reference electrode. The surface area of the various coatings exposed to the NaCl solution was 7 cm^2. EIS spectra were obtained at the open-circuit potential (OCP) across a frequency range of 0.01–100 kHz, with a signal amplitude of 5 mV (root mean square, RMS), and 6 points per decade, after 2 h of immersion. The EIS data were analysed in terms of equivalent electric circuits employing ZSIMPWIN® software (Version 3.50).

2.5.2. Neutral Salt Spray Test

The neutral salt spray test was conducted in accordance with ASTM B117 standards [47], utilising a salt spray chamber manufactured by Ascott Analytical Equipment Limited, Tamworth, U.K. This test served as a method to accelerate the corrosion process. An artificial defect, measuring 3 cm in length and 2 mm in width, was introduced using a metallic knife on various coatings, namely PU, PU/ZnGa-SB, PU/GNR, and PU/ZnGa-SB/GNR coatings. These coatings were positioned in the salt spray chamber and exposed to 5 wt% NaCl fog spray, maintaining a constant humidity of 80% at 40 °C. The extent of damage to the coatings was subsequently documented using the Nikon SMZ25 (Nikon Corporation, Japan) optical microscope.

3. Results and Discussion

3.1. Nanoparticles Characterisation and Microstructure

3.1.1. X-Ray Diffraction Analysis

The crystallinity and phase purity of the synthesised ZnGa-CO_3^{2-}, ZnGa-SB, and ZnGa-SB/GNR were evaluated using XRD analysis as shown in Figure 2a. The XRD pattern of ZnGa-CO_3^{2-} exhibits sharp diffraction peaks at 2θ values of 11.57°, 23.32°, 34.15°, 38.8°, 46.29° and 60.4° corresponding to (003), (006), (012), (015), (018) and (110) crystallographic planes [45]. The ZnGa-SB recorded a similar XRD pattern to that of the ZnGa-CO_3^{2-}, except for one additional peak (♣) at a 2θ value of 5.6°. Subsequently, the d (003) values calculated for both ZnGa-CO_3^{2-} and ZnGa-SB increased from 0.78 nm to 1.57 nm, a change attributed to the larger size of the SB anion [48]. The appearance of the peak (♣) alongside the increased d (003) values confirms the successful intercalation of SB anions into the layers of the ZnGa-SB [49]. While adhering to the required conditions for synthesising ZnGa-SB, it has been noted that the XRD pattern of ZnGa-SB almost aligns with that of ZnGa-CO_3^{2-}. This observation confirms that a higher proportion of CO_3^{2-} anions are present in ZnGa-SB compared to SB anions, owing to the greater affinity of CO_3^{2-} anions for the intermediate layer [50]. The resemblance in the XRD patterns of ZnGa-SB/GNR and ZnGa-SB, with the absence of any distinguishable GNR peaks, indicates the effective wrapping of the GNRs by the ZnGa-SB LDH in the ZnGa-SB/GNR composite [42].

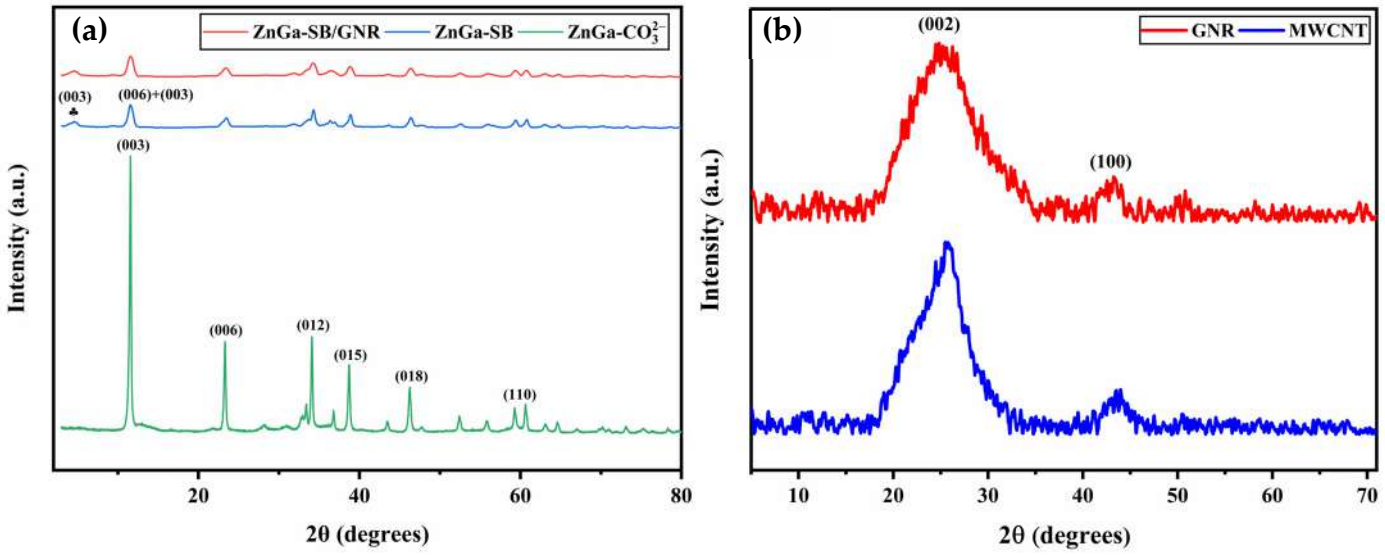

Figure 2. XRD patterns of (**a**) ZnGa-CO_3^{2-}, ZnGa-SB, and ZnGa-SB/GNR, (**b**) MWCNT and GNR.

Additionally, several microstructural parameters were calculated using the obtained XRD data and tabulated in Table 1. The average crystalline size (D) of the nano fillers was calculated using (Equation (1)) the Scherrer equation:

$$D = K\lambda/\beta Cos\theta \quad (1)$$

where β is the full width at half maximum (FWHM) in radian, K is the dimensionless shape factor (0.9), λ is the wavelength of the X-ray used (0.154 nm), and θ is the Bragg's angle.

Table 1. The parameters extracted from XRD data of the synthesised ZnGa-CO_3^{2-}, ZnGa-SB, and ZnGa-SB/GNR samples.

Nanoparticle	β (Radian)	θ (Radian)	D (nm)	ε	δ (10^{15} m^{-2})	γ
ZnGa-CO_3^{2-}	0.0046	0.1007	30.075	0.0114	1.12	0.795
ZnGa-SB	0.0199	0.0495	06.970	0.1004	21.00	1.136
	0.0124	0.0975	11.189	0.0318	08.11	0.808
ZnGa-SB/GNR	0.0205	0.0487	06.767	0.1050	22.30	1.145
	0.0138	0.0965	10.061	0.0357	10.00	0.812

The lattice strain var epsilon (ε) and the dislocation density (δ) from the crystalline size were calculated using Equations (2) and (3)

$$\varepsilon = \beta/4\tan\theta \quad (2)$$

$$\delta = 1/D^2 \quad (3)$$

The stacking fault energy (γ) was calculated using Equation (4)

$$\gamma = 2\pi^2/45\sqrt{3\tan\theta} \quad (4)$$

Figure 2b shows the XRD patterns of MWCNT and GNR. The MWCNTs exhibited two distinct diffraction peaks at 2θ values of 25.7° and 43.3°, respectively. The peak at 25.7° corresponds to the (002) crystallographic plane and the graphitic structure, while the peak at 43.3° is associated with the (100) crystallographic plane, indicative of hexagonal graphite and crystalline order [51]. In contrast, the XRD pattern for GNRs is similar to

that of MWCNTs, but with significantly broader and less intense peaks that are shifted to lower 2θ values. This broadening of the characteristic peaks of GNRs confirms the presence of less crystalline and highly exfoliated GNRs in a few-layer structure, representing a notable reduction from the multi-layered structure of MWCNTs [52]. As shown in Table 2, the interplanar distance for the peak corresponding to the (002) crystallographic plane, calculated using the Bragg equation, is approximately 0.346 nm for MWCNTs and 0.358 nm for GNRs. The lower d-spacing value of MWCNTs (0.346 nm) compared to GNRs (0.358 nm) clearly indicates the incorporation of additional structural defects or oxygen-based functional groups into the GNRs during the oxidative unzipping of MWCNTs, thereby resulting in the increased d-spacing value for GNRs [53,54]. Bragg's equation (Equation (5)) is employed to ascertain the interlayer spacing between the graphitic layers, while the Scherrer-Debye equation (Equation (6)) is utilised to determine the size of the graphitic crystalline structures.

$$d = \lambda/2\mathrm{Sin}(\theta) \quad (5)$$

$$\tau = 0.89\lambda/\beta\mathrm{Cos}(\theta) \quad (6)$$

$$L_x = \tau/d \quad (7)$$

where λ signifies the X-ray's wavelength, β represents the Full Width at Half Maximum (FWHM) peak intensity in radians, and θ is the angle of diffraction. The average number of graphitic layers (L_x) in the nanoparticles was computed by dividing the crystal size by the interlayer spacing (Equation (7)), with the results detailed in Table 2.

Table 2. The parameters extracted from the XRD data of the synthesised MWCNT and GNR samples.

Materials	θ (Radian)	Interplanar Distance (Å)	FWHM (Radian)	τ (Å)	L_x
MWCNT	0.224	3.46	0.1198	11.86	3.427
GNR	0.378	3.58	0.1457	9.73	2.714

3.1.2. FT-IR Analysis

The SB, ZnGa-CO_3^{2-}, ZnGa-SB, and ZnGa-SB/GNR samples were subjected to FT-IR spectroscopy (Figure 3) within the frequency range of 4000 to 500 cm^{-1} to determine the functional groups present in them. The SB spectrum portrays bands at 1549 cm^{-1} and 1411 cm^{-1} that are attributed to the vibrations of the COO^- group, and those at 2923 cm^{-1}, 2849 cm^{-1} and 694 cm^{-1} to the C-H functional group [49]. The ZnGa-CO_3^{2-}, ZnGa-SB, and ZnGa-SB/GNR exhibited a broad band at 3475 cm^{-1} (♥), characteristic of the stretching vibrations of -OH groups within the brucite-like layers of the hydrotalcite-like clay structures, as well as the adsorbed water present in the interlayer region [39]. Besides, for the ZnGa-CO_3^{2-}, the band at 1640–1650 cm^{-1} (♠) is due to the bending vibrations (H-O-H) of the water molecules present in the interlayer of the anionic clay [50]. In addition, the characteristic bands at 1503 cm^{-1}, 1350 cm^{-1} (♣) are ascribed to the stretching vibration of the interlayer CO_3^{2-} anion and the bands below 800 cm^{-1} (♦,●) are due to the lattice vibrations executed by the metal-oxygen functional groups such as M − O, O-M-O, M − OH and M-O-M groups (M = Zn and Ga) [45,55,56]. The FT-IR spectrum of ZnGa-SB exhibits bands corresponding to both SB and ZnGa-CO_3^{2-}, particularly in the frequency range of 1500 cm^{-1} to 2800 cm^{-1}. This observation suggests the possible intercalation of SB into the ZnGa LDH structure. It is crucial to highlight that the spectral profile of ZnGa-SB/GNR remains largely unchanged from that of ZnGa-SB, with the exception of the appearance of relatively broader bands with diminished band intensity.

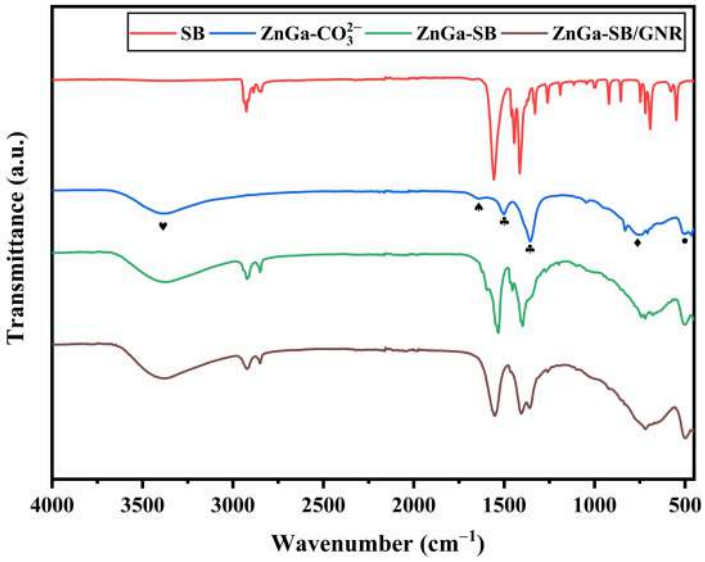

Figure 3. FT-IR spectra of SB, ZnGa-CO_3^{2-}, ZnGa-SB, and ZnGa-SB/GNR.

3.1.3. Raman Spectroscopy

Raman spectroscopy was employed to acquire detailed insights into the structural characteristics of the synthesised carbonaceous materials, i.e., MWCNT and GNR (Figure 4). This technique is crucial for determining the ratio of sp^2 and sp^3 hybridised carbon atoms in the materials under investigation. The Raman spectra of the MWCNT exhibited two distinct peaks at 1320 cm^{-1} and 1590 cm^{-1}. The peak at 1320 cm^{-1}, identified as the D band, is indicative of disordered carbon, corresponding to sp^3 hybridised carbon. Conversely, the peak at 1590 cm^{-1}, termed the G band, is representative of graphitic carbon, reflecting sp^2 hybridised carbon [42]. To assess the structural variations in the carbonaceous materials, the ratio of the D-band intensity to the G-band intensity, i.e., the I_D/I_G ratio, was calculated (Table 3). This ratio provides reliable information about the disorderliness in the particles and the degree of graphitisation [57]. When compared to the MWCNT spectrum, the Raman spectrum of the GNR exhibited a blue shift and broadening of the D band (1340 cm^{-1}) and the G band (1605 cm^{-1}), followed by an increase in the I_D/I_G ratio from 1.1 to 1.4. This increase in the I_D/I_G ratio, along with the blue shift and broadening of the bands, suggests that GNRs possess more defects than MWCNTs, and have a higher number of edges and sites that are conducive to the formation of oxygenated functional groups [53]. Additionally, the inter-defect distance (L_a) for both the MWCNT and GNR was calculated using the Tuinstra & Koenig [52] equation (Equation (8))

$$L_a = 2.4 \times 10^{-10} \times \lambda^4 \times (I_D/I_G)^{-1} \quad (8)$$

where λ is the wavelength of the laser used (633 nm). The GNR exhibited a calculated L_a value of 27.5 nm, which is less than the 35 nm observed for the MWCNT, indicating a higher number of defects on its graphitic structure.

Table 3. The parameters extracted from the Raman data of the synthesised MWCNT and GNR samples.

Materials	I_D/I_G	L_a (nm)
MWCNT	1.1	35
GNR	1.4	27.5

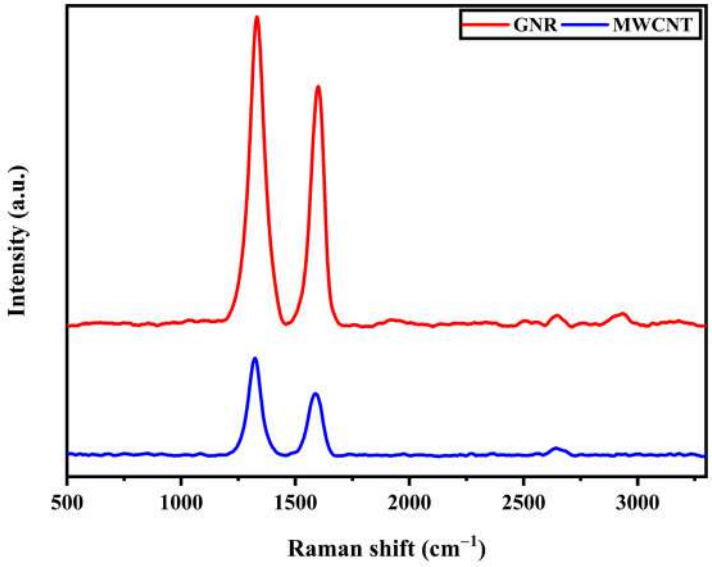

Figure 4. Raman spectra of MWCNT and GNR.

3.1.4. Thermogravimetric Analysis

The thermodynamic stability of the nanoparticles was evaluated using thermogravimetric analysis (TGA) [58]. It has been established that LDHs transition into mixed-metal oxides and spinel phases upon exposure to thermal treatment [59]. Moreover, the TGA profiles for SB, ZnGa-CO_3^{2-}, and ZnGa-SB are illustrated in Figure 5. The TGA curves exhibit two distinct reductions, indicating that this process occurs in two stages. The initial mass reduction was observed within the temperature range of 30 °C to 170 °C, which was attributed to the evaporation of both surface-adsorbed and interlayer water molecules [60], resulting in a 9% decrease in fvfvmass. Subsequently, a further reduction occurred at temperatures above 170 °C, driven by the decomposition of counter anions, the dehydroxylation of brucite layers, and the complete structural collapse [61] of ZnGa-CO_3^{2-}, resulting in an additional 21% mass loss. The overall mass loss of ZnGa-CO_3^{2-}, was approximately 30%, aligning with earlier research on thermal decomposition of LDHs [62]. The TGA curve for SB demonstrates that it undergoes complete decomposition at 480 °C, indicating it is non-hydrated. In comparing the TGA profiles of ZnGa-CO_3^{2-}, and ZnGa-SB, it is apparent that 10% of SB is effectively intercalated within the interlayers of ZnGa-SB.

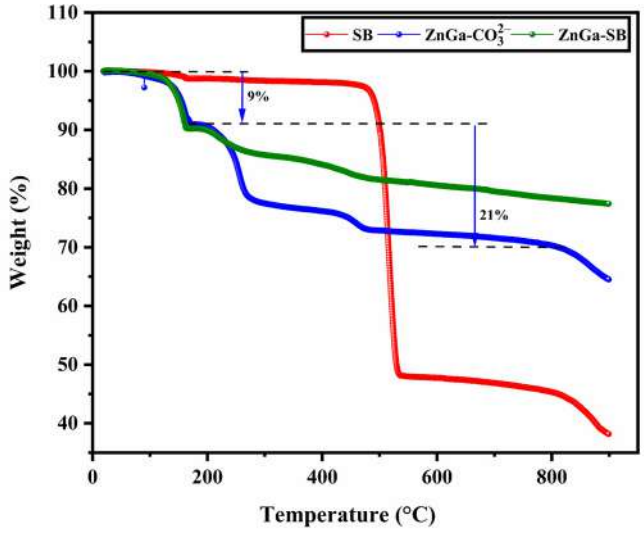

Figure 5. TGA profiles of SB, ZnGa-CO_3^{2-}, and ZnGa-SB.

3.1.5. FE-SEM and EDS Analysis

The surface morphology of the as-synthesised nanofillers was evaluated using a Field Emission Scanning Electron Microscope (FE-SEM). The FE-SEM images of ZnGa-CO_3^{2-}, ZnGa-SB, GNR and ZnGa-SB/GNR are depicted in Figure 6a–d. The FE-SEM image in Figure 6a demonstrates that the ZnGa-CO_3^{2-} particles possess a highly ordered structural arrangement similar to two-dimensional (2D) layers or platelets. As illustrated in Figure 6b, the replacement of CO_3^{2-} anions with SB, led to the crippled and highly distorted plate morphology of ZnGa-SB. The MWCNT particles are characterised by an entangled tubular morphology Figure S1. Following the oxidative unzipping of MWCNTs, the obtained GNRs exhibited a longitudinally unwrapped ribbon morphology, as shown in Figure 6c. Figure 6d illustrates the morphology of the ZnGa-SB/GNR composite, demonstrating that the GNRs are effectively adsorbed onto the surface of the ZnGa-SB plates or sandwiched between them. This configuration facilitates the effective wrapping of GNRs by ZnGa-SB plates, attributed to the strong electrostatic attraction between the negatively charged GNRs and the positively charged ZnGa-SB plates. These results indicate that the incorporation of GNRs with ZnGa-SB effectively prevents the agglomeration of GNRs, suggesting a robust interaction between the ZnGa-SB and GNRs.

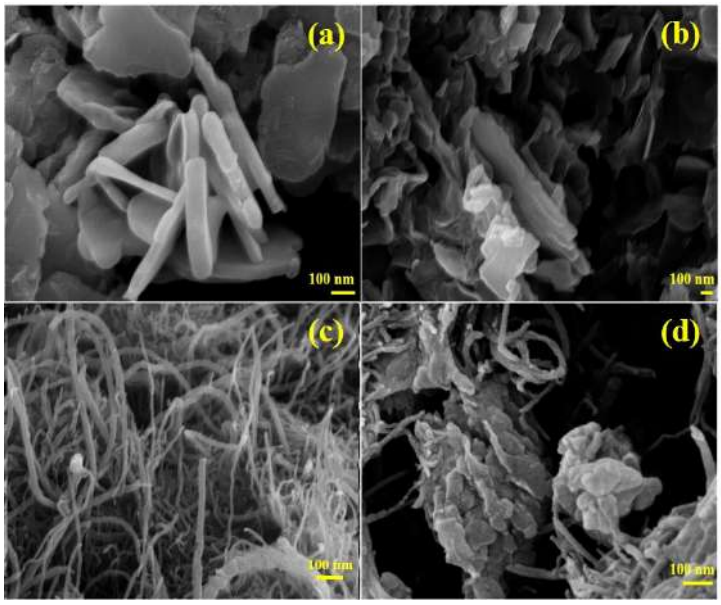

Figure 6. FE-SEM images of (**a**) ZnGa-CO_3^{2-}, (**b**) ZnGa-SB, (**c**) GNR and (**d**) ZnGa-SB/GNR.

Energy dispersive X-ray spectroscopy (EDS) was employed to determine the elemental composition of the synthesised nanofillers. The EDS mapping of the ZnGa-CO_3^{2-}, ZnGa-SB, MWCNT and GNR are depicted in Figure S2. The EDS spectra of both ZnGa-CO_3^{2-} and ZnGa-SB nanofillers reveal the presence of Zn, Ga, C and O elements. Figure S2 illustrates the EDS spectra of MWCNTs and GNRs with C and O elements, demonstrating a notable increase in the O content following the oxidative unzipping of MWCNTs to form GNRs. This observation confirms the successful incorporation of a substantial number of oxygen-containing functional groups onto the surface of the GNRs. Finally, the EDS spectra of ZnGa-SB/GNR, as depicted in Figure 7a–f, confirm the presence of Zn, Ga, C, and O with weight percentages (Figure 7g) of 40.73%, 9.09%, 24.45% and 25.73%, respectively, affirming the purity of the ZnGa-SB/GNR composite.

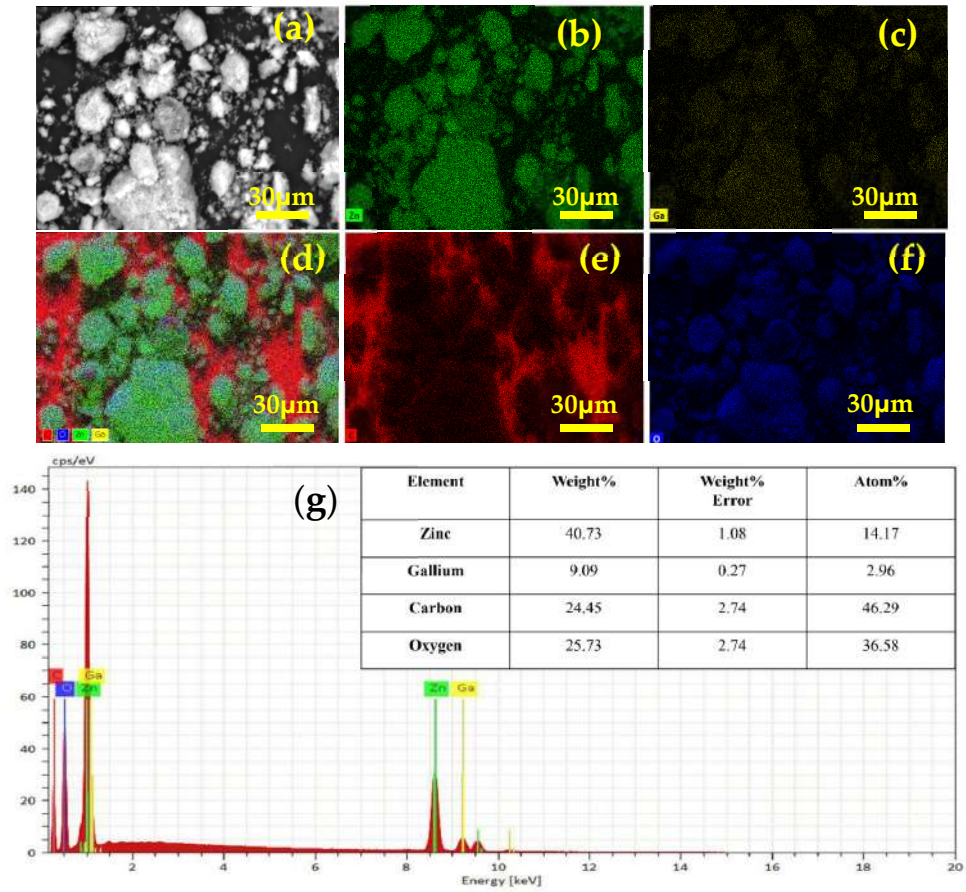

Figure 7. EDS mapping images of (**a**,**d**) ZnGa-SB/GNR with (**b**) Zn, (**c**) Ga, (**e**) C, and (**f**) O distributions and their corresponding (**g**) weight percentages.

3.2. Corrosion Studies

3.2.1. Short-Term Evaluation of Nanofillers

Short-term assessments are essential for understanding the anticorrosive properties of nanofillers, providing a basis for long-term studies. A rapid evaluation method involves incorporating nanofillers into a model organic coating, such as the AC, which serves as a model organic coating for short-term testing. EIS monitoring during immersion in a saline medium is a widely used technique for evaluating the protective capabilities of paints. This technique is also instrumental in evaluating the adhesion properties, barrier effectiveness, and identifying potential defects. The impedance modulus at low frequencies (10^{-2} Hz) in the Bode plot, represented as $|Z|_{0.01}$, can be a significant parameter for estimating the overall protective quality of the coating in certain scenarios [63]. A higher $|Z|_{0.01}$ implies that the coating has better potential to block electron migration and thereby slow the corrosion rate of the steel. The evaluation of the coating's performance was conducted by tracking the changes in its impedance modulus, $|Z|_{0.01}$, over a specified period. The different coatings, namely AC coat, AC/ZnGa-SB, AC/GNR, and AC/ZnGa-SB/GNR, were immersed in 0.1 M NaCl for 0, 2, 6, 12, 24, and 48 h, respectively. The obtained results are represented as Nyquist and Bode plots, as shown in Figure 8a–h. As seen from Figure 9, initially, all coatings, except for the AC/ZnGa-SB/GNR coating, demonstrated $|Z|_{0.01}$ values in the range of 10^6 orders of magnitude. In contrast, the AC/ZnGa-SB/GNR coating exhibited a markedly higher $|Z|_{0.01}$ value of 10^8, exceeding the others by two orders of magnitude. Over time, a reduction in the $|Z|_{0.01}$ values were noted across all coatings. This reduction is attributed to the formation of numerous fine cracks and pores in the top coat during the curing process, which allowed NaCl to infiltrate and diminish the coating's

shielding ability. Notably, at the 12 h mark, the $|Z|_{0.01}$ values of the individual nanofiller-based coatings (AC/ZnGa-SB, AC/GNR) and the AC bare coating converged, indicating the arrival of corrosive species at the doorstop of the base coat. Beyond 24 h, the $|Z|_{0.01}$ value of AC/ZnGa-SB coatings surpassed that of the AC coating, likely due to the simultaneous release of the corrosion inhibitor SB anion and the capture of the Cl^- ions by the ZnGa-SB LDHs. Any further decrease in the $|Z|_{0.01}$ value may be attributed to the incompatibility of ZnGa-SB nanofillers, which compromised their effectiveness in corrosion protection. Subsequently, the AC/GNR coating demonstrated superior anticorrosive properties from 12 h onward, exceeding those of its predecessors by approximately one order of magnitude. This enhancement is attributed to the compatibility of GNRs within AC, which facilitated the creation of an exceptional labyrinth effect. According to various authors [64], two-dimensional structured nanomaterials are capable of filling fine cracks and pores, thereby enhancing the $|Z|_{0.01}$ value, as observed in the case of nanofiller-based coatings (AC/ZnGa-SB, AC/GNR). Ultimately, the AC/ZnGa-SB/GNR coating exhibited the highest $|Z|_{0.01}$ value from the onset of immersion in NaCl (10^8 order magnitude) until 48 hours (10^4 order magnitude). This is because the GNRs served as a physical barrier, effectively slowing down the penetration of corrosive agents due to their extensive specific surface area. The synergistic effect from the ZnGa-SB and GNR nanofillers in the AC/ZnGa-SB/GNR coating played a more effective role in blocking corrosive substances, demonstrating their individual and combined contributions to optimising the interfacial properties and overall performance of such nanofiller-based organic coatings.

3.2.2. EIS of Intact Polyurethane Coatings

EIS was utilised to assess the protective properties of the nanofiller-based coating applied to R36 Q-Panel Steel A1008. Figure 10a–h illustrates the phase angle and Bode modulus plots for the PU bare coat, PU/ZnGa-SB, PU/GNR, and PU/ZnGa-SB/GNR coatings, all of which were immersed in 3.5 wt% NaCl solution at 25 °C for a period of 112 days. The corrosion resistance of these coatings is typically determined by the impedance value at the lowest frequency ($|Z|_{0.01}$ Hz) in the Bode modulus spectra, which is a pivotal indicator of the coating's anticorrosive capabilities [9]. A higher $|Z|_{0.01}$ value is indicative of improved anticorrosion properties. Furthermore, the break-point frequency (f_b), defined as the frequency at which the phase angle spectrum shifts by $-45°$, offers additional insights into the coating's corrosion resistance [65]. Typically, a higher f_b value signifies lower corrosion resistance.

In Figure 11, the PU coating initially presented a $|Z|_{0.01}$ value of 2.94×10^9 Ω cm^2 at the onset of immersion in a 3.5 wt% NaCl solution. As the immersion time progressed, the $|Z|_{0.01}$ value consistently decreased for the PU coating. After 2688 h of immersion, the $|Z|_{0.01}$ value declined markedly to 6.67×10^8 Ω cm^2, signifying a reduction by an order of magnitude. This decline may be attributed to the formation of numerous micropores and cervices resulting from the volatilisation of byproducts during the curing process, which facilitate the pathways for the penetration of Cl^- ions that travel across the coating, leading to substrate corrosion. Furthermore, this decline is reflected in the phase angle plots (Figure 10a), where a significant shift of f_b from the low-frequency to the high-frequency range is observed, indicating a swift progression of corrosion. By the end of the immersion period, f_b reached 0.158 kHz, confirming the deterioration of the barrier properties owing to the permeation of the corrosive solution. Unfortunately, the addition of ZnGa-SB to the PU matrix failed to resolve the coating defects. Initially, the PU/ZnGa-SB coating exhibited a superior $|Z|_{0.01}$ value of 1.18×10^{10} Ω cm^2 at the beginning of immersion in 3.5 wt% NaCl; however, with a prolonged exposure time of 2688 h, the $|Z|_{0.01}$ value drastically declined to 2.38×10^5 Ω cm^2, indicating a complete failure of

the coating (Figures 10d and 11). This five-order magnitude reduction is ascribed to the incompatibility of the ZnGa-SB nanofillers, which negatively impacted the crosslinking degree of the coating. Consequently, f_b in Figure 10c gradually shifted to the high-frequency region due to the reduced relaxation time associated with the infiltration of the electrolyte. In comparison, the PU/GNR coating (Figures 10f and 11) demonstrated an initial $|Z|_{0.01}$ value of 2.27×10^9 Ω cm^2 at 0 h, and a better $|Z|_{0.01}$ value of 5.74×10^6 Ω cm^2 at 2688 h. The one order of magnitude enhancement at 2688 h compared to the PU/ZnGa-SB coating is likely attributed to the incorporation of GNR. The GNR facilitated a labyrinth effect within the PU matrix, thereby enhancing the crosslinking degree of PU-based coatings. Among the nanofiller-based coatings, the PU/ZnGa-SB/GNR coating (Figures 10h and 11) achieved the most favourable $|Z|_{0.01}$ value of 7.10×10^7 Ω cm^2 at 672 h of immersion, compared to its initial $|Z|_{0.01}$ value of 3.18×10^9 Ω cm^2 at 0h, indicating a reduction of only two orders of magnitude. As immersion time increased, a gradual decline in $|Z|_{0.01}$ was noted. At 2688h, the $|Z|_{0.01}$ value remained at 5.90×10^7 Ω cm^2, despite an increased f_b value, underscoring the durability of the PU/ZnGa-SB/GNR coating. The integration of ZnGa-SB and GNR resulted in a synergistic enhancement of corrosion inhibition facilitated by the release of SB, its ion exchangeability with Cl^- ions, and an intensified labyrinth effect, collectively strengthening the physical barrier properties of the PU/ZnGa-SB/GNR coating. Furthermore, the inherent stability of the GNRs significantly contributed to the extended durability of the PU/ZnGa-SB/GNR coating.

Electrical equivalent circuit models were employed to interpret the EIS results of the intact coating, allowing for a thorough investigation of the electrochemical process and enabling a quantitative analysis. Pearson's values (χ^2) for all the data that were fitted were less than or equal to 10^{-3}, indicating a strong correlation between the fitted results and the EIS data. The selection of equivalent electrical circuits was guided by existing literature and the characteristics of the Nyquist plot, Bode plot, and the specific system under study [58]. As the corrosive agent infiltrates the coating and initiates metal corrosion, leading to coating degradation, two time constants become evident at this phase, illustrated by two impedance arcs in the Nyquist diagram. Thus, an equivalent circuit with two time constants, i.e., $R_s(Q_c(R_c(Q_{dl}R_{ct})))$, was employed to fit the EIS data (Figure S3). One time constant pertains to the passivation film on the carbon steel surface in a highly alkaline solution, while the other is associated with the electrochemical corrosion process at the solution/substrate interface [64,66]. The fitted parameters are tabulated in Table 4. Constant phase elements (CPEs) are represented by the pre-factor of the CPE (Q), which accounts for their non-ideal capacitive nature. The equivalent coating capacitance (C_c) and the double-layer capacitance (C_{dl}) were determined using Equation (9), which involves the admittance (Y_o) and the phase shift coefficient (n). R_c and R_{ct} represent the coating's resistance to ion diffusion and charge transfer at the interface, respectively, both of which are critical to corrosion protection [67,68].

$$C_{c/dl} = \frac{(Y_o \times R_{c/ct})^{1/n}}{R_{c/ct}} \text{ where } n = 0 \leq 1 \quad (9)$$

As illustrated in Table 4, the R_{ct} and R_c values of all the coatings diminished at varying rates as immersion time increased, indicating the infiltration of corrosive species into the coatings at different rates. Initially, the PU coating exhibited R_c (3.61×10^7 Ω cm^2) and R_{ct} (1.23×10^{11} Ω cm^2) values at 0 h, which gradually decreased to R_c (8.54×10^6 Ω cm^2) and R_{ct} (4.61×10^9 Ω cm^2) at 672 h. Ultimately, the PU coating achieved values of R_c (1.51×10^6 Ω cm^2) and R_{ct} (1.33×10^{10} Ω cm^2) at the conclusion of 2688 h. This observation confirms the superior barrier properties of the PU coating for R36 Q-Panel Steel. Conversely, the PU/ZnGa-SB coating initially recorded the R_c (3.02×10^7 Ω cm^2) and

R_{ct} (4.69×10^{10} Ω cm^2) values at 0 h. However, the PU/ZnGa-SB coating failed to sustain these high values, with R_c (2.40×10^4 Ω cm^2) and R_{ct} (7.21×10^5 Ω cm^2) values significantly reduced at 2688 h, indicating limited durability in the NaCl solution. The R_c (3.08×10^7 Ω cm^2) and R_{ct} (6.84×10^{10} Ω cm^2) values for PU/GNR coating at 0 h are comparable to those of the PU coating. At the end of 2688 h, R_c (5.71×10^5 Ω cm^2) and R_{ct} (2.96×10^7 Ω cm^2) values were observed for PU/GNR coating. The one order of magnitude reduction in the R_c value compared to the PU coating suggests that GNR nanofillers provide enhanced efficacy among the previously discussed nanofiller-based coatings. Notably, the PU/ZnGa-SB/GNR coating exhibits improved R_c (4.01×10^7 Ω cm^2) and R_{ct} (8.97×10^{10} Ω cm^2) values at 0 h. Even after 2688 h of immersion, the R_c and R_{ct} values of the PU/ZnGa-SB/GNR coating remain notably high at 7.13×10^6 Ω cm^2 and 4.32×10^8 Ω cm^2, respectively. The $|Z|_{0.01}$, R_c, and R_{ct} recorded for the PU/ZnGa-SB/GNR are good compared to those already reported [7,69–72] for anticorrosive organic coatings (Table S1). These findings emphasise the PU/ZnGa-SB/GNR coating's outstanding barrier capabilities in shielding the R36 Q-Panel Steel against corrosive attack. By serving as a robust physical barrier, this coating markedly impedes the inward diffusion of corrosive species, thereby preventing charge transfer at the interface between the coating and R36 Q-Panel Steel.

3.2.3. Neutral Salt Spray Analysis

Neutral Salt Spray Analysis (NSSA) was employed to evaluate the anticorrosion properties of the PU, PU/ZnGa-SB, PU/GNR, and PU/ZnGa-SB/GNR coatings, in accordance with ASTM B117 guidelines. The coatings were exposed to a 5 wt% saline fog (pH = 7) at 40 °C and a constant humidity of 80% for 360 h. Figure 12 illustrates the optical images of various coatings at intervals of 0 h, 168 h, and 360 h, respectively. It is well established from the EIS evaluation that intact coatings show no signs of corrosion. Consequently, to stimulate mechanical damage, a 3 cm horizontal incision was made on the surface of the different coatings using a sterile blade, before exposure to the saline fog environment. Rust formation was distinctly observed around the scratch for all coatings after 168 h of exposure, with deterioration continuing over time. As illustrated in Figure 12, after 168 h, the PU/ZnGa-SB/GNR coating exhibited the lowest level of corrosion, whereas the PU/ZnGa-SB coating showed significant corrosion. The corrosion rates of the PU and PU/GNR coatings were nearly identical. Following prolonged exposure to the saline environment, at 360 h, the PU coating displayed cathodic delamination and numerous corrosion products around the scratched area Figure 13. In the case of the PU/ZnGa-SB coating, severe deterioration was observed around the scratch, which was attributed to the limited protective efficacy of the sole ZnGa-SB nanofillers in retarding the initiation and progression of corrosion at the scratched site. Another contributing factor could be the incompatibility of ZnGa-SB nanofillers with the PU, creating defects that facilitate the ingress of corrosive species. Subsequently, the PU/GNR coating exhibited a significant reduction in the formation of corrosion products around the scratch compared to the PU/ZnGa-SB coating; however, a large number of blisters and corrosion spots were observed, likely due to their hydrophilic nature and penetration of corrosive agents into the interface between the metal and PU coating. Moreover, the PU/ZnGa-SB/GNR coating demonstrated minimal corrosion products and nearly no blisters around the scratch or across the entire coating surface. This outcome was attributed to the release of SB, entrapment of chloride ions, and enhanced labyrinth effect facilitated by the ZnGa-SB/GNR nanofillers. These findings confirm the superior potency of the ZnGa-SB/GNR nanofillers in enhancing the anticorrosion properties of the PU coatings.

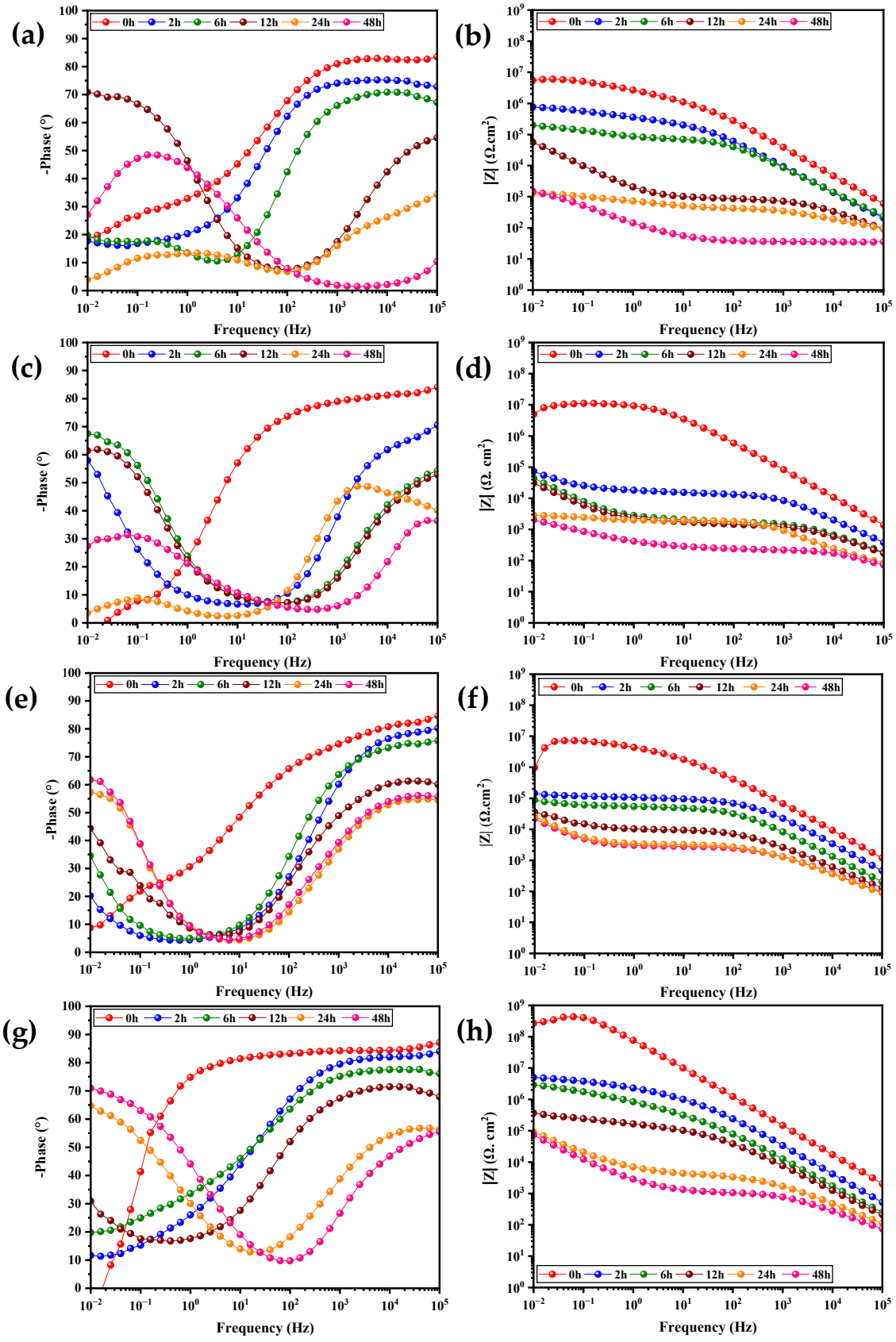

Figure 8. Bode impedance modulus and the Bode phase spectra of (**a**,**b**) AC, (**c**,**d**) AC/ZnGa-SB, (**e**,**f**) AC/GNR, and (**g**,**h**) AC/ZnGa-SB/GNR coatings immersed in 0.1 M NaCl solution.

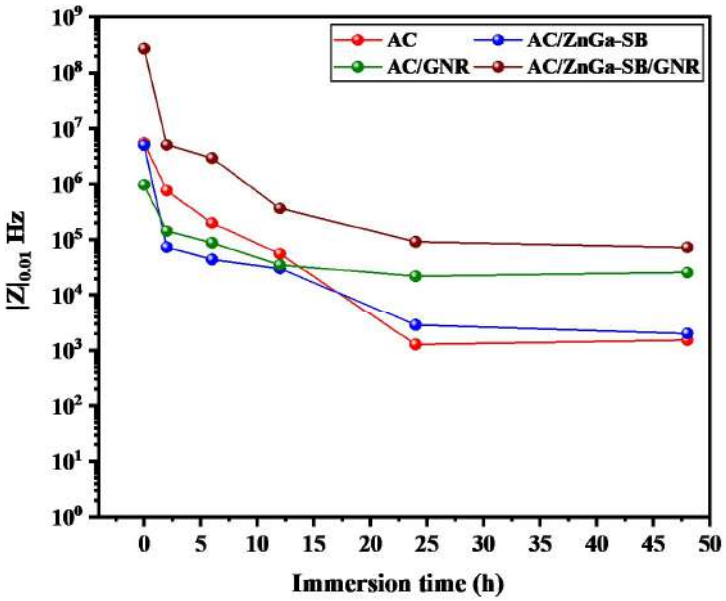

Figure 9. $|Z|_{0.01}$ values of AC, AC/ZnGa-SB, AC/GNR, and AC/ZnGa-SB/GNR coatings immersed in 0.1 M NaCl solution at different time intervals.

3.2.4. Crosshatch Adhesion Test

The adhesion strength of the different coatings, namely the PU base coat, PU/ZnGa-SB, PU/GNR, and PU/ZnGa-SB/GNR, applied to the steel substrate was evaluated using the cross-cut test, in accordance with the guidelines specified in ISO 2409:2020 (E) [73]. The assessment was performed qualitatively through visual inspection. The thickness of these coatings varied between 65 and 75 µm, requiring a cut spacing of 2 mm in each direction to form a lattice pattern. Any remaining loose paint in the cut area was brushed off. Subsequently, the centre of the 3M tape was precisely aligned over the lattice, and the tape was smoothed. After a five-minute duration, the 3M tape was detached by grasping the free end and pulling it away at a 60 ° angle. Any instances of peeling or detachment were assessed using the reference criteria [72,74] outlined in Table 5. This table delineates levels ranging from 0 to 5, with level 0 indicating the strongest adhesion between the coating and substrate. As seen in Figure 14a–h, the lattice squares in all the coatings remained intact without any detachment, and the edges of the cuts remained smooth. These observations demonstrate the exceptional adhesion of the coatings to the substrate.

3.2.5. Pencil Hardness Test

The film hardness of an organic coating on a metal was determined using a rapid and inexpensive pencil test, as described in ISO 15184 [75]. The coated panels (PU base coat, PU/ZnGa-SB, PU/GNR, and PU/ZnGa-SB/GNR) were placed on a firm horizontal surface. The flattened pencil tip was held firmly against the film at a 45° angle (point away from the operator), exerting a force of 7.35 ± 0.15 N, and pushed away from the operator for a minimum of 5 mm. The hardness of the pencil lead (6B, 5B, 4B, 3B, 2B, B, HB, F, H, 2H, 3H, 4H, 5H, and 6H) increased in steps until the surface of the coating was marked by visible defects. The test began with the softest pencil, 6B, and progressed to the hardest pencil, 6H. The test result was the highest hardness at which no markings occurred. The damage is assessed using an optical microscope after cleaning the pencil fragments from the paint surface with a cotton swab immersed in an inert solvent compatible with the coating. Figures S4–S6 and 15 show the optical microscopic images of the PU, PU/ZnGa-SB, PU/GNR, and PU/ZnGa-SB/GNR coatings subjected to the pencil hardness test. The PU coating showed no visible traces or damage from pencils graded 6B to F, suggesting

that these pencils traversed the coating surface without resistance. Conversely, pencils graded from H to 6H produced noticeable scratches. However, the remaining coatings, that is, PU/ZnGa-SB, PU/GNR, and PU/ZnGa-SB/GNR coatings, shielded themselves from any possible damage until the pencil grade H and began to show increasing traces of damage from pencil grades 2H to 6H. This observation suggests that the H-grade pencil was the last to leave the surface unmarked, underscoring the superior hardness of the nanofiller-based coating.

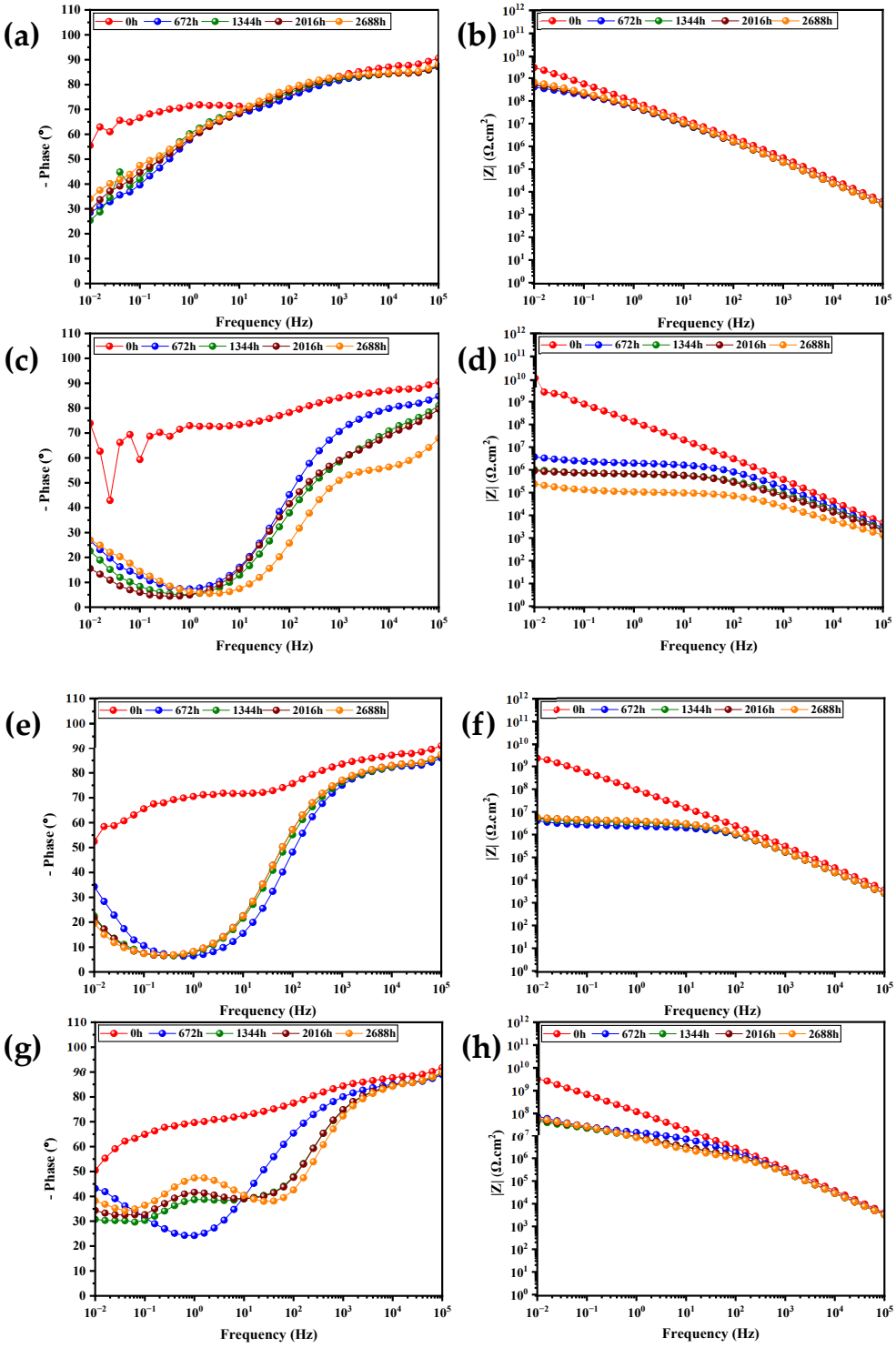

Figure 10. Bode impedance modulus and the Bode phase spectra of (**a**,**b**) PU, (**c**,**d**) PU/ZnGa-SB, (**e**,**f**) PU/GNR, and (**g**,**h**) PU/ZnGa-SB/GNR coatings immersed in 3.5 wt% NaCl solution.

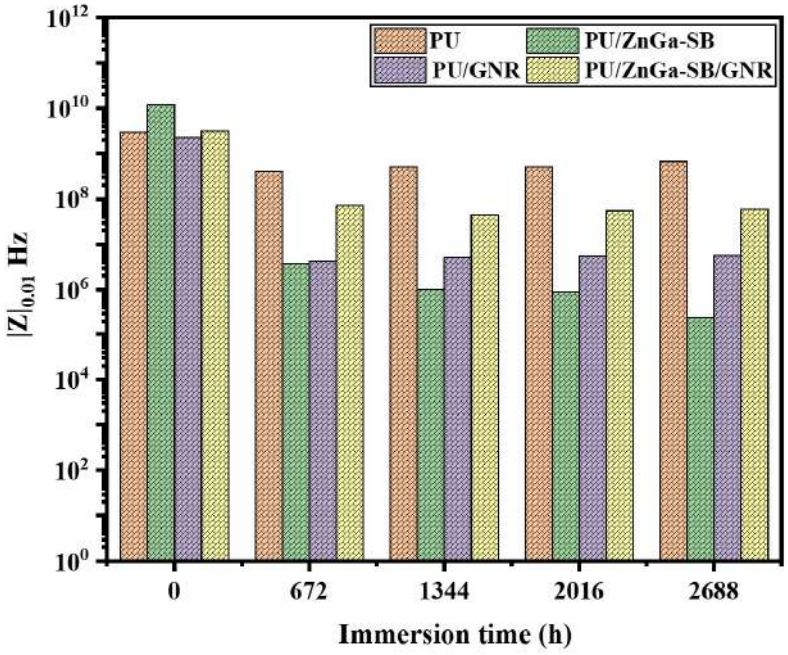

Figure 11. $|Z|_{0.01}$ values of PU, PU/ZnGa-SB, PU/GNR, and PU/ZnGa-SB/GNR coatings immersed in 3.5 wt% NaCl solution at different time intervals.

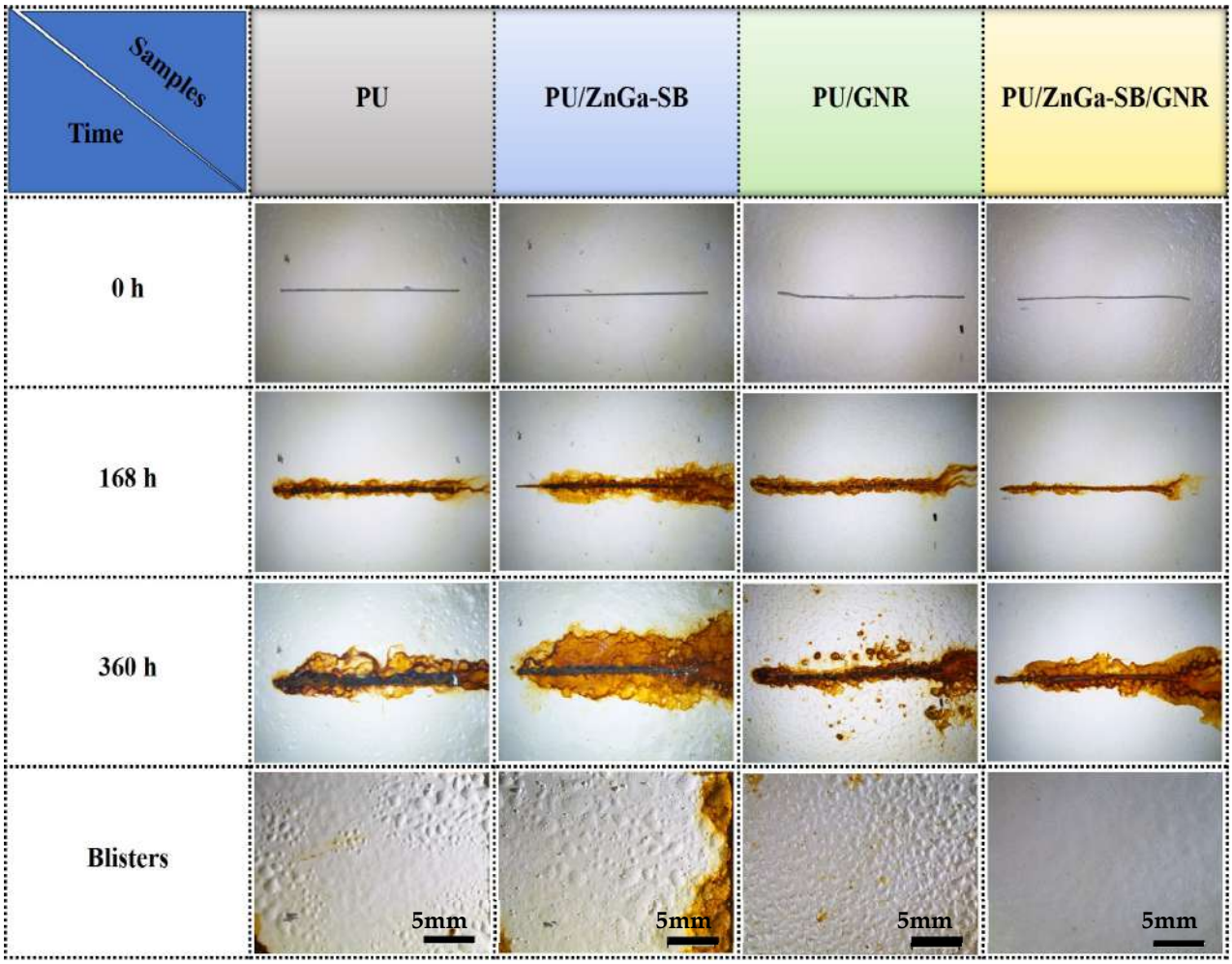

Figure 12. Images of scratched PU, PU/ZnGa-SB, PU/GNR, and PU/ZnGa-SB/GNR coatings after the preset exposure periods to the neutral salt spray test.

Table 4. Impedance parameters of the PU-coated samples at different immersion periods in 3.5 wt % NaCl solution at 25 °C.

Coatings	Immersion Time (h)	CPE_c (S s^n cm^{-2})		C_c (F cm^2)	R_c (Ω cm^2)	CPE_{dl} (S s^n cm^{-2})		C_{dl} (F cm^2)	R_{ct} (Ω cm^2)	χ^2 (Chi-Square)
		Y_o	n			Y_o	n			
PU	0	9.57×10^{-11}	0.96	8.32×10^{-10}	3.61×10^{7}	2.70×10^{-10}	0.71	1.13×10^{-9}	1.23×10^{11}	5.96×10^{-4}
	672	1.80×10^{-10}	0.94	1.19×10^{-10}	8.54×10^{6}	7.19×10^{-10}	0.53	2.08×10^{-9}	4.61×10^{9}	1.44×10^{-3}
	1344	1.85×10^{-10}	0.94	1.26×10^{-10}	1.27×10^{7}	6.18×10^{-10}	0.53	2.05×10^{-9}	6.25×10^{9}	1.45×10^{-3}
	2016	1.87×10^{-10}	0.94	1.29×10^{-10}	1.66×10^{7}	6.92×10^{-10}	0.50	4.14×10^{-9}	8.65×10^{9}	3.12×10^{-4}
	2688	1.56×10^{-10}	0.95	1.01×10^{-10}	1.51×10^{6}	6.28×10^{-10}	0.51	4.83×10^{-9}	1.33×10^{10}	2.85×10^{-4}
PU/ZnGa-SB	0	8.67×10^{-11}	0.96	6.77×10^{-11}	3.02×10^{7}	2.54×10^{-10}	0.67	8.61×10^{-10}	4.69×10^{10}	4.45×10^{-4}
	672	1.96×10^{-10}	0.93	9.50×10^{-11}	3.40×10^{5}	3.12×10^{-9}	0.48	1.08×10^{-10}	1.44×10^{7}	3.98×10^{-3}
	1344	8.83×10^{-11}	1.00	8.83×10^{-11}	5.52×10^{4}	4.98×10^{-9}	0.62	5.00×10^{-10}	4.72×10^{6}	6.51×10^{-4}
	2016	2.24×10^{-10}	0.94	1.13×10^{-10}	9.91×10^{4}	5.94×10^{-9}	0.61	6.17×10^{-10}	4.87×10^{6}	3.78×10^{-3}
	2688	3.46×10^{-10}	0.93	1.43×10^{-10}	2.40×10^{4}	1.29×10^{-8}	0.66	1.16×10^{-9}	7.21×10^{5}	2.05×10^{-3}
PU/GNR	0	9.39×10^{-11}	0.96	7.36×10^{-11}	3.08×10^{7}	2.83×10^{-10}	0.69	1.07×10^{-9}	6.84×10^{10}	1.13×10^{-3}
	672	2.53×10^{-10}	0.91	9.02×10^{-11}	1.17×10^{5}	1.55×10^{-8}	0.47	5.32×10^{-9}	2.50×10^{7}	3.87×10^{-3}
	1344	1.97×10^{-10}	0.94	1.09×10^{-10}	4.89×10^{5}	2.57×10^{-9}	0.45	9.41×10^{-11}	2.60×10^{7}	2.33×10^{-3}
	2016	1.85×10^{-10}	0.94	1.03×10^{-10}	5.86×10^{5}	2.03×10^{-9}	0.47	8.39×10^{-11}	2.92×10^{7}	4.47×10^{-4}
	2688	1.87×10^{-10}	0.94	1.04×10^{-10}	5.71×10^{5}	2.12×10^{-9}	0.46	8.22×10^{-11}	2.96×10^{7}	2.39×10^{-4}
PU/ZnGa-SB/GNR	0	8.03×10^{-11}	0.97	6.72×10^{-11}	4.01×10^{7}	2.29×10^{-10}	0.68	9.50×10^{-10}	8.97×10^{10}	7.12×10^{-4}
	672	1.12×10^{-10}	0.96	8.85×10^{-11}	3.11×10^{7}	2.47×10^{-9}	0.39	7.32×10^{-10}	1.86×10^{8}	2.05×10^{-3}
	1344	1.32×10^{-10}	0.95	9.13×10^{-11}	6.86×10^{6}	6.58×10^{-9}	0.49	2.28×10^{-8}	5.01×10^{8}	6.02×10^{-4}
	2016	1.34×10^{-10}	0.95	9.35×10^{-11}	7.94×10^{6}	5.96×10^{-9}	0.53	1.73×10^{-8}	5.59×10^{8}	3.32×10^{-4}
	2688	1.39×10^{-10}	0.94	8.94×10^{-11}	7.13×10^{6}	5.53×10^{-9}	0.61	9.65×10^{-9}	4.32×10^{8}	4.15×10^{-3}

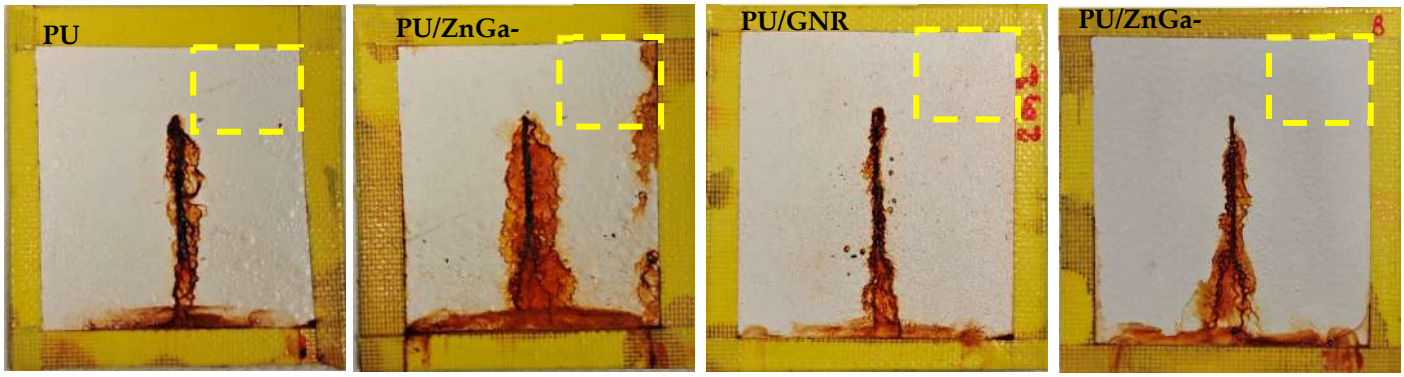

Figure 13. Images of scratched PU, PU/ZnGa-SB, PU/GNR, and PU/ZnGa-SB/GNR coatings after 360 h of exposure to the neutral salt spray test, showing blisters.

Table 5. ISO 2409:2020 (E) standard adhesion rating system, including descriptions and the percentage of coating detachment.

Classification	Description	Appearance
0	The edges of the cuts are completely smooth, and none of the squares of the lattice is detached.	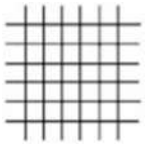
1	Detachment of small flakes of the coating at the intersections of the cuts. A cross-cut area of no more than 5% is affected.	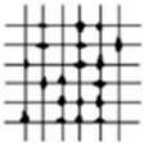
2	The coating has flaked along the edges and/or at the intersections of the cuts. A cross-cut area greater than 5%, but not greater than 15%, is affected.	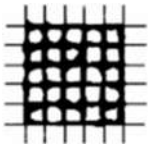
3	The coating has flaked along the edges of the cuts partly or wholly in large ribbons, and/or it has flaked partly or wholly on different parts of the squares. A cross-cut area greater than 15%, but not greater than 35%, is affected.	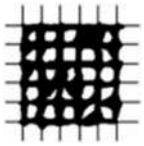
4	The coating has flaked along the edges of the cuts in large ribbons, and/or some squares have partially or wholly detached. A cross-cut area greater than 35%, but not greater than 65%, is affected.	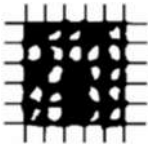
5	Any degree of flaking that cannot even be classified by classification 4.	-

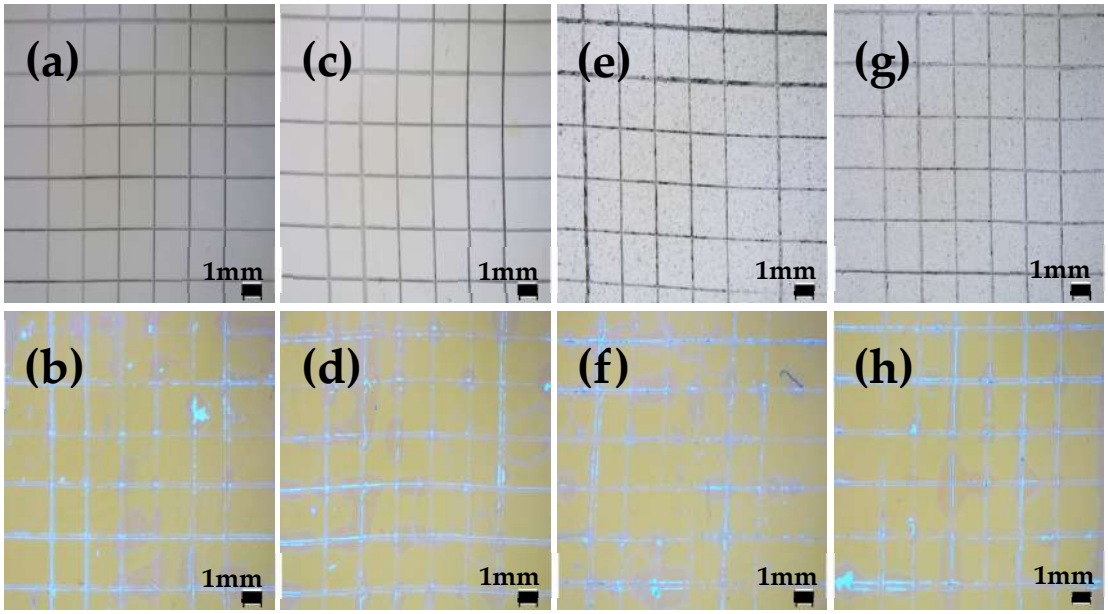

Figure 14. Images of (**a**,**b**) PU, (**c**,**d**) PU/ZnGa-SB, (**e**,**f**) PU/GNR and (**g**,**h**) PU/ZnGa-SB/GNR coatings after the crosshatch tape test and the corresponding crosshatch tapes, respectively.

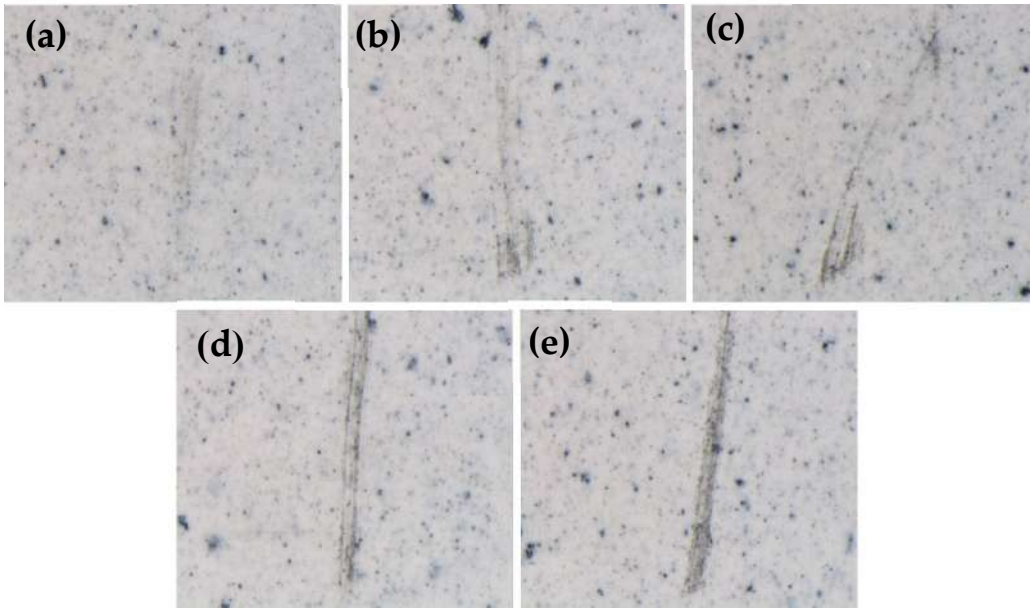

Figure 15. Optical images of the damage caused by the (**a**) 2H, (**b**) 3H, (**c**) 4H, (**d**) 5H and (**e**) 6H pencils for PU/ZnGa-SB/GNR coating during the pencil hardness test.

4. Conclusions

The ZnGa-CO_3^{2-}, ZnGa-SB, GNR, and ZnGa-SB/GNR hybrid nanofillers were synthesised via an in situ hydrothermal method and incorporated into PU coatings. Extensive physical and chemical characterisation confirmed the successful formation of various nanofillers and the intercalation of SB into the LDH interlayers. The short-term screening of acrylic coatings showed enhanced barrier performance for ZnGa-SB/GNR, with a $|Z|_{0.01}$ value of 7.3×10^4 Ω cm^2 in 0.1 M NaCl. Long-term EIS evaluation in 3.5 wt% NaCl showed sustained corrosion protection for PU/ZnGa-SB/GNR, with $|Z|_{0.01}$, R_c, and R_{ct} values of 5.90×10^7 Ω cm^2, 7.13×10^6 Ω cm^2, and 4.32×10^8 Ω cm^2, respectively. Neutral salt spray tests confirmed minimal corrosion products and blister-free surfaces for PU/ZnGa-SB/GNR, affirming its superior anticorrosion performance. All coatings

incorporating nanofillers demonstrated improved mechanical properties, promoting better adhesion strength and film hardness.

The enhanced protective capabilities of nanofiller-incorporated coatings stem from a significant synergistic mechanism across structural, chemical, and electrochemical dimensions of the coating system. Structurally, this synergy is evident as the GNR is sandwiched between the ZnGa-SB layers, creating a complex, multilayered barrier that effectively impedes corrosive elements. From a chemical and electrochemical standpoint, the synergy is demonstrated through the integration of active and passive inhibition mechanisms. The ZnGa–SB LDH possesses ion-exchange capabilities, allowing it to absorb Cl^- ions and release SB, while simultaneously providing Zn and Ga-based species that contribute to the formation of robust passivation layers. Together, these synergetic effects enhance corrosion resistance and durability, positioning ZnGa-SB/GNR as a promising candidate for anticorrosive PU coatings.

Supplementary Materials: The following supporting information can be downloaded at: https://www.mdpi.com/article/10.3390/pr14030400/s1. Figure S1: FE-SEM image of MWCNT; Figure S2: EDS mapping results of (a) ZnGa-CO_3^{2-}, (b) ZnGa-SB, (c) MWCNT and (d) GNR; Figure S3: Nyquist plots of (a,b) PU, (c,d) PU/ZnGa-SB, (e,f) PU/GNR and (g,h) PU/ZnGa-SB/GNR coatings fitted with $R_s(Q_c(R_c(Q_{dl}R_{ct})))$ model using ZSimp software; Figure S4: Optical images of the damage caused by the (a) H, (b) 2H, (c) 3H, (d) 4H, (e) 5H and (f) 6H pencils for PU coating during the pencil hardness test; Figure S5: Optical images of the damage caused by the (a) 2H, (b) 3H, (c) 4H, (d) 5H, and (e) 6H pencils for PU/ZnGa-SB coating during the pencil hardness test.; Figure S6: Optical images of the damage caused by the (a) 2H, (b) 3H, (c) 4H, (d) 5H, and (e) 6H pencils for PU/GNR coating during the pencil hardness test; Table S1: Comparison table depicting state-of-the-art corrosion-resistant coatings reported in recent literature with our work. Refs. [7,69–72] are cited in Supplementary Materials.

Author Contributions: Conceptualization, U.M.P., M.F., and S.R.; methodology, U.M.P. and M.F.; software, U.M.P.; validation, M.F., S.R.; formal analysis, U.M.P., M.F. and S.R.; investigation, U.M.P.; resources, S.R., M.F.; data curation, U.M.P.; writing—original draft preparation, U.M.P.; writing—review and editing, U.M.P., M.F., and S.R.; visualization, U.M.P., S.R., and M.F.; supervision, S.R., M.F.; project administration, S.R., M.F.; funding acquisition, S.R., M.F. All authors have read and agreed to the published version of the manuscript.

Funding: This research received no external funding.

Data Availability Statement: The original contributions presented in this study are included in the article/Supplementary Material. Further inquiries can be directed to the corresponding author.

Acknowledgments: The authors gratefully acknowledge Paolo Bettotti, University of Trento, for his assistance with Raman analysis and Luca Benedetti, University of Trento, for his assistance with FE-SEM and FT-IR analysis.

Conflicts of Interest: The authors declare that they have no conflicts of interest.

References

1. Nguyen, T.D.; Nguyen, A.S.; Tran, B.A.; Vu, K.O.; Tran, D.L.; Phan, T.T.; Scharnagl, N.; Zheludkevich, M.L.; To, T.X.H. Molybdate intercalated hydrotalcite/graphene oxide composite as corrosion inhibitor for carbon steel. *Surf. Coat. Technol.* **2020**, *399*, 126165. [CrossRef]
2. Zhang, M.; Xu, F.; Lin, D.; Peng, J.; Zhu, Y.; Wang, H. A smart anti-corrosion coating based on triple functional fillers. *Chem. Eng. J.* **2022**, *446*, 137078. [CrossRef]

3. Ji, X.; Seif, A.; Duan, J.; Rashidi, A.; Zhou, Z.; Pourhashem, S.; Mirzaee, M.; Zhai, X.; Zhao, X.; Hou, B. Experimental and DFT studies on corrosion protection performance of epoxy/graphene quantum dots@TiO_2 nanotubes coatings. *Constr. Build. Mater.* **2022**, *322*, 126501. [CrossRef]
4. Zehra, S.; Mobin, M.; Parveen, M.; Ahmad, R. Corrosion Fundamentals: Understanding the Science Behind the Damage. In *Industrial Corrosion: Fundamentals, Failure, Analysis and Prevention*; Wiley: Hoboken, NJ, USA, 2025; pp. 1–16. [CrossRef]
5. Anjum, M.J.; Zhao, J.; Zahedi Asl, V.; Yasin, G.; Wang, W.; Wei, S.; Zhao, Z.; Qamar Khan, W. In-situ intercalation of 8-hydroxyquinoline in Mg-Al LDH coating to improve the corrosion resistance of AZ31. *Corros. Sci.* **2019**, *157*, 1–10. [CrossRef]
6. Danaee, I.; Darmiani, E.; Rashed, G.R.; Zaarei, D. Self-healing and anticorrosive properties of Ce(III)/Ce(IV) in nanoclay–epoxy coatings. *Iran. Polym. J.* **2014**, *23*, 891–898. [CrossRef]
7. Zhong, F.; He, Y.; Wang, P.; Chen, C.; Xie, P.; Li, H.; Chen, J. One-step hydrothermal synthesis of reduced graphene oxide/aspartic acid intercalated layered double hydroxide for enhancing barrier and self-healing properties of epoxy coating. *React. Funct. Polym.* **2019**, *145*, 104380. [CrossRef]
8. Tabish, M.; Zhao, J.; Kumar, A.; Yan, J.; Wang, J.; Shi, F.; Zhang, J.; Peng, L.; Mushtaq, M.A.; Yasin, G. Developing epoxy-based anti-corrosion functional nanocomposite coating with CaFe-Tolyl-triazole layered double hydroxide@g-C_3N_4 as nanofillers on Q235 steel substrate against NaCl corrosive environment. *Chem. Eng. J.* **2022**, *450*, 137624. [CrossRef]
9. Li, H.; Qiang, Y.; Zhao, W.; Zhang, S. 2-Mercaptobenzimidazole-inbuilt metal-organic-frameworks modified graphene oxide towards intelligent and excellent anti-corrosion coating. *Corros. Sci.* **2021**, *191*, 109715. [CrossRef]
10. Liu, Y.; Shi, W.; Li, L.; Wei, W.; Wang, H.; Xu, Y.; Yang, X.; Dong, S. "One Stone Three Birds": A self-healing polyurethane multifunctional composite coating with favorable photothermal effect, anti-corrosion and anti-cavitation. *Appl. Surf. Sci.* **2026**, *718*, 164948. [CrossRef]
11. Kiani, S.; Haddadi-Asl, V.; Khosravi, A.; Eivaz Mohammadloo, H.; Ahmadi, H. Designing a smart polyurethane anti-corrosion coating loaded with APTES/IMZ modified halloysite nanotubes. *Surf. Coat. Technol.* **2024**, *492*, 131179. [CrossRef]
12. Wang, L.; Li, S.N.; Fu, J.J. Self-healing anti-corrosion coatings based on micron-nano containers with different structural morphologies. *Prog. Org. Coat.* **2023**, *175*, 107381. [CrossRef]
13. Nawaz, M.; Yusuf, N.; Habib, S.; Shakoor, R.A.; Ubaid, F.; Ahmad, Z.; Kahraman, R.; Mansour, S.; Gao, W. Development and properties of polymeric nanocomposite coatings. *Polymers* **2019**, *11*, 852. [CrossRef] [PubMed]
14. Attaei, M.; Calado, L.M.; Morozov, Y.; Taryba, M.G.; Shakoor, R.A.; Kahraman, R.; Marques, A.C.; Montemor, M.F. Smart epoxy coating modified with isophorone diisocyanate microcapsules and cerium organophosphate for multilevel corrosion protection of carbon steel. *Prog. Org. Coat.* **2020**, *147*, 105864. [CrossRef]
15. Ramezanzadeh, B.; Akbarian, M.; Ramezanzadeh, M.; Mahdavian, M.; Alibakhshi, E.; Kardar, P. Corrosion Protection of Steel with Zinc Phosphate Conversion Coating and Post-Treatment by Hybrid Organic-Inorganic Sol-Gel Based Silane Film. *J. Electrochem. Soc.* **2017**, *164*, C224–C230. [CrossRef]
16. Zhang, Y.; Shao, Y.; Zhang, T.; Meng, G.; Wang, F. The effect of epoxy coating containing emeraldine base and hydrofluoric acid doped polyaniline on the corrosion protection of AZ91D magnesium alloy. *Corros. Sci.* **2011**, *53*, 3747–3755. [CrossRef]
17. Hao, Y.; Liu, F.; Han, E. Inhibitive Behavior and Mechanism of a Ferrite Inhibition Pigment in Epoxy Paints. *J. Electrochem. Soc.* **2012**, *159*, C403–C410. [CrossRef]
18. Behzadnasab, M.; Mirabedini, S.M.; Kabiri, K.; Jamali, S. Corrosion performance of epoxy coatings containing silane treated ZrO_2 nanoparticles on mild steel in 3.5% NaCl solution. *Corros. Sci.* **2011**, *53*, 89–98. [CrossRef]
19. Zahidah, K.A.; Kakooei, S.; Ismail, M.C.; Bothi Raja, P. Halloysite nanotubes as nanocontainer for smart coating application: A review. *Prog. Org. Coat.* **2017**, *111*, 175–185. [CrossRef]
20. Hayatdavoudi, H.; Rahsepar, M. Smart inhibition action of layered double hydroxide nanocontainers in zinc-rich epoxy coating for active corrosion protection of carbon steel substrate. *J. Alloys Compd.* **2017**, *711*, 560–567. [CrossRef]
21. Chen, T.; Chen, R.; Jin, Z.; Liu, J. Engineering hollow mesoporous silica nanocontainers with molecular switches for continuous self-healing anticorrosion coating. *J. Mater. Chem. A* **2015**, *3*, 9510–9516. [CrossRef]
22. Blustein, G.; Di Sarli, A.R.; Jaén, J.A.; Romagnoli, R.; Del Amo, B. Study of iron benzoate as a novel steel corrosion inhibitor pigment for protective paint films. *Corros. Sci.* **2007**, *49*, 4202–4231. [CrossRef]
23. Sinko, J. Challenges of chromate inhibitor pigments replacement in organic coatings. *Prog. Org. Coat.* **2001**, *42*, 267–282. [CrossRef]
24. Cao, Y.; Zheng, D.; Li, X.; Lin, J.; Wang, C.; Dong, S.; Lin, C. Enhanced Corrosion Resistance of Superhydrophobic Layered Double Hydroxide Films with Long-Term Stability on Al Substrate. *ACS Appl. Mater. Interfaces* **2018**, *10*, 15150–15162. [CrossRef] [PubMed]
25. Ding, C.; Tai, Y.; Wang, D.; Tan, L.; Fu, J. Superhydrophobic composite coating with active corrosion resistance for AZ31B magnesium alloy protection. *Chem. Eng. J.* **2019**, *357*, 518–532. [CrossRef]

26. Dong, Y.; Wang, F.; Zhou, Q. Protective behaviors of 2-mercaptobenzothiazole intercalated Zn-Al-layered double hydroxide coating. *J. Coat. Technol. Res.* **2014**, *11*, 793–803. [CrossRef]
27. Wang, Y.; Yuan, Z.; Zhang, Z.; Xin, Y.; Fujita, T.; Wei, Y. In situ one-step fabrication of superhydrophobic layered double hydroxide on Al alloys for anti-corrosion. *Appl. Surf. Sci.* **2022**, *593*, 153400. [CrossRef]
28. Wu, H.; Zhang, Y.; Long, S.; Zhang, L.; Jie, X. Tribological behavior of graphene anchored Mg-Al layered double hydroxide film on Mg alloy pre-sprayed Al coating. *Appl. Surf. Sci.* **2020**, *530*, 146536. [CrossRef]
29. Shen, G.; Zhang, L.; Gu, Z.; Zheng, Z.; Liu, Y.; Tan, G.; Jie, X. Zinc aluminum-layered double hydroxide(LDH)-graphene oxide(GO) lubricating and corrosion-resistant composite coating on the surface of magnesium alloy. *Surf. Coat. Technol.* **2022**, *437*, 128354. [CrossRef]
30. Xue, K.; Xing, M.; Chen, T.; Xi, B.; Zhang, H.; Ye, K.; Feng, J.; Qian, W.; Qiu, J.; Liu, X. Mg-Ga layered double hydroxides coating endow magnesium with antibacterial and osteogenic properties for guided-bone regeneration application. *J. Mater.* **2025**, *11*, 101071. [CrossRef]
31. Chen, R.; Xu, Y.; Xie, X.; Li, C.; Zhu, W.; Xiang, Q.; Li, G.; Wu, D.; Li, X.; Wang, L. Synthesis of TiO_2 nanotubes/nickel-gallium layered double hydroxide heterostructure for highly-efficient photocathodic anticorrosion of 304 stainless steel. *Surf. Coat. Technol.* **2021**, *424*, 127641. [CrossRef]
32. Akman, A.; Alberta, L.A.; Giraldo-Osorno, P.M.; Turner, A.B.; Hantusch, M.; Palmquist, A.; Trobos, M.; Calin, M.; Gebert, A. Effect of minor gallium addition on corrosion, passivity, and antibacterial behaviour of novel β-type Ti–Nb alloys. *J. Mater. Res. Technol.* **2023**, *25*, 4110–4124. [CrossRef]
33. Chung, Y.; Lee, C.-W. Electrochemistry of Gallium. *J. Electrochem. Sci. Technol.* **2013**, *4*, 1–18. [CrossRef]
34. Rezaeifard, S.; Shahrabi, T.; Ramezanzadeh, B. Emerging Mo-doped MgAl-LDH lamellar/carbon nanotubes as 3D sustainable nanohybrid for designing a durable smart anti-corrosion composite. *Surf. Coat. Technol.* **2024**, *488*, 131013. [CrossRef]
35. Cristoforetti, A.; Rossi, S.; Deflorian, F.; Fedel, M. Unlocking the Potential of Sebacate: Investigating Its Role in the Inhibition of Filiform Corrosion on Organic Coated Steel. *Metals* **2024**, *14*, 623. [CrossRef]
36. Hefter, G.T.; North, N.A.; Tan, S.H. Organic Corrosion Inhibitors in Neutral Solutions; Part 1—Inhibition of Steel, Copper, and Aluminum by Straight Chain Carboxylates. *Corrosion* **1997**, *53*, 657–667. [CrossRef]
37. Rammelt, U.; Koehler, S.; Reinhard, G. Electrochemical characterisation of the ability of dicarboxylic acid salts to the corrosion inhibition of mild steel in aqueous solutions. *Corros. Sci.* **2011**, *53*, 3515–3520. [CrossRef]
38. Lahem, D.; Poelman, M.; Atmani, F.; Olivier, M.G. Synergistic improvement of inhibitive activity of dicarboxylates in preventing mild steel corrosion in neutral aqueous solution. *Corros. Eng. Sci. Technol.* **2012**, *47*, 463–471. [CrossRef]
39. Cristoforetti, A.; Parola, F.; Parrino, F.; Izquierdo, J.; Souto, R.M.; Rossi, S.; Deflorian, F.; Fedel, M. Sebacate intercalated Ca–Al layered double hydroxide pigments for corrosion protection of low carbon steel: Anion exchange and electrochemical properties. *Appl. Clay Sci.* **2024**, *250*, 107300. [CrossRef]
40. Stimpfling, T.; Leroux, F.; Hintze-Bruening, H. Organo-modified layered double hydroxide in coating formulation to protect AA2024 from corrosion. *Colloids Surf. A Physicochem. Eng. Asp.* **2014**, *458*, 147–154. [CrossRef]
41. Wang, X.; Zhu, J.; Lei, Y.; Lei, W. Synthesis and characterization of layered double hydroxides hybrid microcapsules for anticorrosion via self-healing and chloride ion adsorption. *Appl. Clay Sci.* **2022**, *221*, 106481. [CrossRef]
42. Rezaeifard, S.; Shahrabi, T.; Ramezanzadeh, B. Trisodium phosphate-loaded magnesium-aluminum layered double hydroxides/oxidized-multiwalled carbon nanotubes self-assembled 2D-nanohybrid for designing a multifunctional smart epoxy nanocomposite. *Appl. Clay Sci.* **2024**, *254*, 107376. [CrossRef]
43. Swamy, N.K.; Mohana, K.N.S.; Hegde, M.B.; Madhusudana, A.M. Fabrication of 1D graphene nanoribbon and malenized linseed oil-based nanocomposite: A highly impervious bio-based anti-corrosion coating material for mild steel. *J. Appl. Electrochem.* **2022**, *52*, 1133–1148. [CrossRef]
44. Ansell, P.; Berry, L.; Mcgettrick, J.; Searle, J.; Wint, N. Role of Smart-Release Pigments in Preventing Corrosion Driven Cathodic Disbondment of Organically Coated Hot Dip Galvanised Steel. *J. Electrochem. Soc.* **2023**, *170*, 011502. [CrossRef]
45. Ding, W.; Luo, J.-X.; Gu, Q.; Liu, Z.H. Ultrathin 2D ZnGa-borate-LDH nanosheets for boosting dye-sensitized photocatalytic coupled reaction of H_2 production with pollutant degradation. *Colloids Surf. A Physicochem. Eng. Asp.* **2023**, *657*, 130575. [CrossRef]
46. Kosynkin, D.V.; Higginbotham, A.L.; Sinitskii, A.; Lomeda, J.R.; Dimiev, A.; Price, B.K.; Tour, J.M. Longitudinal unzipping of carbon nanotubes to form graphene nanoribbons. *Nature* **2009**, *458*, 872–876. [CrossRef]
47. *ASTM B117-19*; Standard Practice for Operating Salt Spray (Fog) Apparatus. ASTM International: West Conshohocken, PA, USA, 2019; pp. 1–15. [CrossRef]
48. Souza, L.H.d.O.; Cristoforetti, A.; Cotting, F.; Reis da Costa Campos, W.; Rossi, S.; Fedel, M. Sebacate-Intercalated CaAl-LDH Pigments for Corrosion Protection of Aluminum Alloy. *ACS Omega* **2025**, *10*, 59771–59781. [CrossRef]

49. Nguyen, D.T.; To, H.T.X.; Gervasi, J.; Paint, Y.; Gonon, M.; Olivier, M.G. Corrosion inhibition of carbon steel by hydrotalcites modified with different organic carboxylic acids for organic coatings. *Prog. Org. Coat.* **2018**, *124*, 256–266. [CrossRef]
50. Caballero, D.; Beltrán-Cobos, R.; Tavares, F.; Cruz-Yusta, M.; Granados, L.S.; Sánchez-Moreno, M.; Pavlovic, I. The Inhibitive Effect of Sebacate-Modified LDH on Concrete Steel Reinforcement Corrosion. *ChemEngineering* **2022**, *6*, 72. [CrossRef]
51. Huang, C.; Zhang, M.; Li, C. A novel non-enzymatic electrochemical glucose sensors based on graphene oxide nanoribbons: Tracking energy expenditure and nutritional intake in sports. *Alex. Eng. J.* **2024**, *89*, 184–194. [CrossRef]
52. Habibpour, S.; Um, J.G.; Jun, Y.-S.; Bhargava, P.; Park, C.B.; Yu, A. Structural Impact of Graphene Nanoribbon on Mechanical Properties and Anti-corrosion Performance of Polyurethane Nanocomposites. *Chem. Eng. J.* **2021**, *405*, 126858. [CrossRef]
53. Heiba, A.R.; Abou Shahba, R.M.; Dhmees, A.S.; Taher, F.A.; El Sawy, E.N. Graphene oxide nanoribbons (GONRs) as pH-tolerant electrodes for supercapacitors: Effect of charge carriers and loading. *J. Energy Storage* **2024**, *83*, 110762. [CrossRef]
54. Heiba, A.R.; Omran, M.M.; Abou Shahba, R.M.; Dhmees, A.S.; Taher, F.A.; El Sawy, E. Compositing LaSrMnO3 perovskite and graphene oxide nanoribbons for highly stable asymmetric electrochemical supercapacitors. *Mater. Sci. Energy Technol.* **2025**, *8*, 82–95. [CrossRef]
55. Wu, S.; Liang, H.; Zhang, Z.; Zhang, Q.; Han, Q.; Wang, J.; Gao, M.; Fan, H.; Yang, J.; Lang, J. The photocatalytic degradation and mechanism of rhodamine B by Zn–Al layered double hydroxide. *Opt. Mater.* **2022**, *131*, 112636. [CrossRef]
56. Singh, K.S.; Sawant, S.G. Identification of $CaCO_3$ polymorphs of shellfish by FTIR spectroscopy and evaluation of metals adsorption by powdered exoskeleton shell. *Indian J. Geo-Marine Sci.* **2022**, *51*, 304–309. [CrossRef]
57. Dehghani, A.; Sanaei, Z.; Fedel, M.; Ramezanzadeh, M.; Mahdavian, M.; Ramezanzade, B. Fabrication of an intelligent anti-corrosion silane film using a MoO_4^{2-} loaded Micro/mesoporous ZIF67-MOF/multi-walled-CNT/APTES core-shell nano-container. *Colloids Surf. A Physicochem. Eng. Asp.* **2023**, *656*, 130511. [CrossRef]
58. Majidi, R.; Danaee, I.; Vrsalović, L.; Zarei, D. Development of a smart anticorrosion epoxy coating containing a pH-sensitive GO/MOF nanocarrier loaded with 2-mercaptobenzothiazole corrosion inhibitor. *Mater. Chem. Phys.* **2023**, *308*, 128291. [CrossRef]
59. Stanimirova, T.; Piperov, N.; Petrova, N.; Kirov, G. Thermal evolution of Mg-Al-CO_3 hydrotalcites. *Clay Miner.* **2004**, *39*, 177–191. [CrossRef]
60. Zhou, L.; Zhang, Q.; Feng, X.; Rui, Z.; Guo, W.; Zhang, Y.; Li, W.; Li, Z. Chloride ion-responsive active protection epoxy composite coatings realized by 2-Mercaptobenzimidazole and 2-Mercaptobenzothiazole intercalated Mg-Al layered double hydroxides. *Corros. Sci.* **2024**, *234*, 112144. [CrossRef]
61. Jaśkaniec, S.; Hobbs, C.; Seral-Ascaso, A.; Coelho, J.; Browne, M.P.; Tyndall, D.; Sasaki, T.; Nicolosi, V. Low-temperature synthesis and investigation into the formation mechanism of high quality Ni-Fe layered double hydroxides hexagonal platelets. *Sci. Rep.* **2018**, *8*, 4179. [CrossRef] [PubMed]
62. Ma, W.; Ma, R.; Wang, C.; Liang, J.; Liu, X.; Zhou, K.; Sasaki, T. A superlattice of alternately stacked Ni-Fe hydroxide nanosheets and graphene for efficient splitting of water. *ACS Nano* **2015**, *9*, 1977–1984. [CrossRef]
63. Rammelt, U.; Reinhard, G. Application of electrochemical impedance spectroscopy (EIS) for characterizing the corrosion-protective performance of organic coatings on metals. *Prog. Org. Coat.* **1992**, *21*, 205–226. [CrossRef]
64. Guo, H.; Yang, C.; Sun, H.; Xiang, N.; Li, C.; Wang, C. Silane coupling agent modified layered double hydroxide/graphene oxide preparation of intelligent anticorrosive coating. *Surf. Coat. Technol.* **2023**, *467*, 129728. [CrossRef]
65. Su, Y.; Qiu, S.; Wei, J.; Zhu, X.; Zhao, H.; Xue, Q. Sulfonated polyaniline assisted hierarchical assembly of graphene-LDH nanohybrid for enhanced anticorrosion performance of waterborne epoxy coatings. *Chem. Eng. J.* **2021**, *426*, 131269. [CrossRef]
66. Wang, J.; Cao, Y.; Xue, J.; Zhang, X.; Liang, Y.; Chen, K.; Huang, C.; Zheng, D. A comparative experimental and theoretical calculation study of CaAl-LDH modified with various aromatic inhibitors for corrosion protection study in epoxy coatings. *Corros. Sci.* **2024**, *231*, 111994. [CrossRef]
67. Shoar Abouzari, M.R.; Berkemeier, F.; Schmitz, G.; Wilmer, D. On the physical interpretation of constant phase elements. *Solid State Ion.* **2009**, *180*, 922–927. [CrossRef]
68. Harsha, Y.M.; Mohana, K.N.S.; Sunilkumar, M.C.; Hithesh, M.C.; Sreelakshmi, M.; Madhusudhana, A.M. Syntheses of diphenolic resin based anti-corrosion coating material and reinforce its performance through MWCNT-Ag and MWCNT-Ag/PANI nanofillers. *Surf. Coat. Technol.* **2024**, *485*, 130871. [CrossRef]
69. Guan, J.; Du, X. Utilizing the synergistic effect of CNT and graphene hybrid fillers to improve the anticorrosion performance of Zn/epoxy coatings. *Mater. Today Commun.* **2025**, *49*, 114029. [CrossRef]
70. AitAghzzaf, A.; Zarki, Y.; Rhouta, B.; Khalil, A.; Veys-Renaux, D.; Majdoub, H.; Rocca, E. Intercalation of decanoate anions (C10) in layered double hydroxide Mg–Al and its application as controlled-release corrosion inhibitor of steel. *Surf. Coatings Technol.* **2024**, *489*, 131055. [CrossRef]

71. Li, J.; Wang, D.; Hou, L.; Zhang, S.; Wu, P.; Zhang, Y.; Liu, B.; Wei, Y. Enhancing the corrosion resistance of the epoxy coating using CaAl LDH intercalated with L-cysteine and its derivatives as a pigment on steel substrate. *Prog. Org. Coat.* **2024**, *193*, 108527. [CrossRef]
72. Mukunda Murthy, K.N.; Shivaswamy, M.B.; Sanjana, M.S.; Kavyashree, M.B.; Sangamesha, M.A.; Deepak Raj, G.R.; Nagendra Prasad, H.S. CuO@Bi_2MoO_6 heterojunction nanocomposite-reinforced epoxy coating: Enhanced anti-corrosion performance on low-carbon steel. *Mater. Today Commun.* **2025**, *49*, 113790. [CrossRef]
73. *ISO 2409*; Paints and Varnishes—Cross-Cut Test. ISO: Geneva, Switzerland, 2020.
74. Zhang, Q.; Yu, Y.; Li, J.; Yin, C.; Tian, F.; Liu, J.; Zhou, J. Synergistic Corrosion Inhibition and UV Protection via TTA-Loaded LDH Nanocontainers in Epoxy Coatings. *Coatings* **2025**, *15*, 505. [CrossRef]
75. *STN EN ISO 15184*; Paints and Varnishes-Determination of Film Hardness by Pencil Test. Slovak Office of Standards, Metrology and Testing: Bratislava, Slovakia, 2021.